

A space-time extension of a conservative two-fluid cut-cell method for moving diffusion problems

Louis Libat ^{*1}, Can Selçuk¹, Eric Chénier¹, and Vincent Le Chenadec¹

¹MSME, Université Gustave Eiffel, UMR CNRS 8208, Marne-la-Vallée, 77454, France

January 1, 2026

Abstract

We present a space-time extension of a conservative Cartesian cut-cell finite-volume method for two-phase diffusion problems with prescribed interface motion. The formulation follows a two-fluid approach: one scalar field is solved in each phase with discontinuous material properties, coupled by sharp interface conditions enforcing flux continuity and jump laws. To handle moving boundaries on a fixed Cartesian grid, the discrete balance is written over phase-restricted space-time control volumes, whose geometric moments (swept volumes and apertures) are used as weights in the finite-volume operators. This construction naturally accounts for the creation and destruction of cut cells (fresh/dead-cell events) and yields strict discrete conservation. The resulting scheme retains the algebraic structure of the static cut-cell formulation while incorporating motion through local geometric weights and interface coupling operators. A series of verification and validation tests in two and three dimensions demonstrate super-linear accuracy in space, robust behavior under repeated topology changes and conservation across strong coefficient jumps and moving interfaces. The proposed space-time cut-cell framework provides a conservative building block for multiphase transport in evolving geometries and a foundation for future free-boundary extensions such as Stefan-type phase change.

1 Introduction

Two-phase scalar transport with sharp interface conditions in temperature or concentration underpins a wide range of natural and industrial processes, from solidification and melting in metallurgical applications to reactive separations and dissolution problems in chemical engineering [2]. In such settings, two media with distinct material properties (e.g. diffusivity, capacity, solubility) are separated by a moving boundary across which the scalar field may remain continuous or may satisfy partition laws, while the diffusive flux obeys a conservation constraint. Predictive simulation therefore hinges on the ability to enforce these jump and continuity relations sharply, while preserving the local balance of the transported quantity.

A central numerical difficulty is geometric: the relevant physics often concentrates in the vicinity of material boundaries, where large gradients and boundary fluxes control the global exchange rates. This is well known in boundary-dominated flow and transport configurations, for instance when viscous stresses and pressure drag are set by near-wall dynamics or when conjugate heat transfer near solid surfaces controls thermal loads in engineering devices. In diffusion-dominated multiphase problems, the same observation holds: accuracy and robustness are largely determined by how the method represents curved boundaries and how it enforces interfacial fluxes.

Body-fitted discretizations can represent boundaries accurately but they typically require mesh motion and/or remeshing when interfaces deform or translate, which complicates robustness, conservation and automation. Unstructured techniques can conform to complex geometries and are very effective for general shapes, including (piecewise) curved surfaces [10], but high-quality mesh generation remains challenging and time-consuming and the explicit storage of element connectivity increases both algorithmic complexity and computational cost [13]. These limitations are one of two compelling arguments for

^{*}Corresponding author: louis.libat2@univ-eiffel.fr

structured Cartesian meshes, the second being the simplicity and efficiency of many solvers and data structures on such grids.

This has motivated fixed-grid approaches where the interface is embedded in a Cartesian background mesh. On non-conforming grids, immersed-boundary and ghost-cell techniques enforce boundary and interface constraints by modifying stencils or introducing forcing terms [16, 17, 6, 7]. Diffuse-interface variants were historically popular in immersed-boundary formulations [17] and have been generalized through fictitious domain and Lagrange-multiplier strategies [8, 20]. While these approaches are attractive for their flexibility, they may compromise strict local conservation or introduce small but systematic errors near the interface when strong coefficient jumps are present.

Embedded-boundary (cut-cell) finite-volume methods provide an alternative that is particularly well suited to diffusion-dominated transport. In cut-cell approaches, the physical control volumes are obtained by intersecting Cartesian cells with the true geometry and the discrete equations are derived directly from integral balances so that conservation is enforced by construction. Pioneering Cartesian embedded-boundary formulations for elliptic operators were proposed by Johansen and Colella [11] and extended to finite-volume advection-diffusion in irregular domains by Calhoun et al. [3]. For diffusion and Poisson problems, conservative cut-cell schemes and accurate boundary-flux reconstructions have been developed and analyzed in a variety of configurations [15, 18, 14]. These results make cut-cell discretizations an appealing foundation for two-phase scalar transport: they naturally incorporate discontinuous material properties, enforce boundary conditions through physical fluxes on embedded faces and recover standard second-order formulas away from the boundary while preserving local conservation in strongly irregular cut cells. Moreover, the underlying two-fluid Cartesian cut-cell framework has already been developed and validated [12] for fixed-boundary diffusion problems, including sharp interface coupling and conservative flux enforcement on embedded boundaries.

The situation becomes substantially more delicate when the interface moves. As the geometry evolves, the cut-cell volumes and face apertures vary in time, and cells can suddenly appear or disappear as the boundary sweeps through the mesh (the fresh and dead cut-cell events [5]). Without a consistent treatment of these geometric changes, purely spatial formulations can exhibit spurious gain or loss of scalar mass/energy. This issue is closely related to the geometric conservation law on moving meshes [5] and has been addressed in several moving-boundary and fluid-structure contexts [9]. From the viewpoint of conservation, a natural remedy is to formulate the method directly in space-time: balances are written over swept control volumes on each time slab, so that changes in volume and aperture are accounted for by construction through a discrete Reynolds transport theorem and an exact geometric conservation law.

Following Tarzia's terminology [21], two-phase diffusion problems can be classified into three categories: (i) *fixed-boundary problems*, where the geometry is time-independent and only classical boundary conditions (Dirichlet/Neumann/Robin) or jumps law on static material interfaces must be enforced; (ii) *moving-boundary problems*, where the interface motion is prescribed (e.g. translating, oscillating or rigid-body kinematics), which already induces repeated cut-cell topology changes; (iii) *free-boundary problems*, where the interface position is part of the solution, as in Stefan-type phase change driven by a latent-heat balance [19, 1]. The present paper targets the intermediate but essential setting (ii): prescribed motion of a sharp interface, viewed as a controlled environment to design and validate conservative space-time operators that will also be required for future free-boundary (Stefan) extensions.

We present a space-time extension of a conservative two-fluid cut-cell diffusion method for moving geometries. The guiding principle is to retain the simplicity and efficiency of a Cartesian background mesh, while representing the moving interface sharply through phase-restricted control volumes and enforcing coupling through local jump operators. Geometrically, the method relies on a finite set of robust moments (volumes, apertures, centroids and staggered moments as needed) computed from intersection operations; these geometric fields are the only inputs required to modify the standard finite-volume formulas in the vicinity of the moving boundary and the operators degenerate to their classical mesh-aligned counterparts when the interface aligns with grid faces.

The main contributions are:

- A space-time finite-volume formulation on phase-restricted control volumes, in which the scalar balance is enforced over swept space-time regions so that geometric changes (fresh/dead cut cells) are handled conservatively by construction.
- A two-fluid interface treatment that preserves sharp jump/continuity conditions using local coupling operators supported by cut-cell geometric weights, allowing discontinuous diffusivities and interfacial transfer laws to be enforced without smearing.

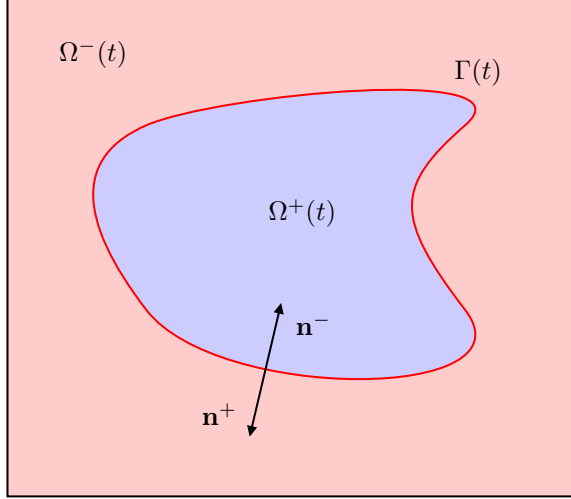


Figure 1: Fixed background domain Ω with a prescribed moving interface $\Gamma(t)$ partitioning Ω into $\Omega^-(t)$ and $\Omega^+(t)$. Normals \mathbf{n}^\pm point outward of their respective phases.

- A practical implementation strategy based on robust geometric moments and intersection operations, suitable for repeated prescribed interface motion on a Cartesian mesh.

The remainder of the paper is organized as follows. Section 2 introduces the two-fluid diffusion model, the jump and boundary conditions and the prescribed kinematics of the moving interface. Sections 3 and 4 detail the construction of phase-restricted geometric moments and discrete operators and derive the space-time cut-cell finite-volume discretization. Section 5 presents numerical experiments and convergence studies. Conclusions and perspectives are provided in Section 6.

2 Continuum modeling

We consider diffusive transfers between two immiscible phases in a fixed background domain $\Omega \subset \mathbb{R}^d$ ($d \in \{1, 2, 3\}$). The geometry evolves in time through a prescribed sharp interface $\Gamma(t)$ that partitions Ω into two time-dependent subdomains occupied by the red and blue phases, denoted $\Omega^-(t)$ and $\Omega^+(t)$, respectively (Figure 1). The immiscibility and saturation conditions read

$$\Omega^-(t) \cap \Omega^+(t) = \emptyset, \quad (1)$$

$$\Omega^-(t) \cup \Gamma(t) \cup \Omega^+(t) = \Omega. \quad (2)$$

Superscripts “-” and “+” denote phase-wise quantities and \mathbf{n}^\pm are the unit normals on $\Gamma(t)$ pointing outward of $\Omega^\pm(t)$. We take the red phase as reference and define $\mathbf{n} := \mathbf{n}^-$ on $\Gamma(t)$. The interface motion is prescribed through an interfacial velocity $\mathbf{w}(t, \mathbf{x})$, with normal component

$$w(t, \mathbf{x}) := \mathbf{w}(t, \mathbf{x}) \cdot \mathbf{n}(t, \mathbf{x}), \quad \mathbf{x} \in \Gamma(t). \quad (3)$$

In this work, $\Gamma(t)$ (and thus w) is given and the transport problem is solved on the evolving domains $\Omega^\pm(t)$.

2.1 Bulk transport equations

Let ϕ denote a generic scalar (temperature T or concentration c). In each phase, ϕ^\pm satisfies the diffusion balance

$$C^\pm \frac{\partial \phi^\pm}{\partial t} + \nabla \cdot \mathbf{q}^\pm = r^\pm, \quad t > 0, \quad \mathbf{x} \in \Omega^\pm(t), \quad (4)$$

closed by a purely diffusive constitutive law (Fourier/Fick),

$$\mathbf{q}^\pm := -K^\pm \nabla \phi^\pm. \quad (5)$$

Here C^\pm denotes the capacity (e.g. $\rho^\pm c_p^\pm$ for heat, ρ^\pm for species) and K^\pm the mobility (e.g. k^\pm or D^\pm). In the present study, C^\pm and K^\pm are taken constant within each phase to retain a linear bulk operator; r^\pm denotes a volumetric source term. Initial conditions are prescribed at $t = 0$ on $\Omega^\pm(0)$.

2.2 Interfacial conditions

We recall the definition of the λ -weighted jump at an interfacial point $\mathbf{x} \in \Gamma(t)$ by

$$[\![\phi]\!]^\lambda(t, \mathbf{x}) := \lim_{\varepsilon \rightarrow 0^+} \left[\phi^+(t, \mathbf{x} - \varepsilon \mathbf{n}^+(t, \mathbf{x})) - (\lambda \phi^-)(t, \mathbf{x} - \varepsilon \mathbf{n}^-(t, \mathbf{x})) \right]. \quad (6)$$

When $\lambda \equiv 1$, we recover the standard jump notation $[\![\phi]\!] := [\![\phi]\!]^1$.

Conservation at the moving interface (neglecting interfacial storage, line fluxes and interfacial sources) yields the continuity of the normal flux in the interface frame. With w defined by (3), this reads

$$[\![\mathbf{q} \cdot \mathbf{n} - C \phi w]\!](t, \mathbf{x}) = 0, \quad t > 0, \quad \mathbf{x} \in \Gamma(t). \quad (7)$$

The term $C \phi w$ accounts for the transport of ϕ induced by the motion of the interface and is the key contribution distinguishing the moving-geometry setting from the static one.

Equation (7) must be complemented by an additional interfacial law to close (4). Since $\Gamma(t)$ is prescribed here, a single scalar relation is sufficient. For conjugate heat transfer one typically enforces continuity (possibly with a prescribed jump f),

$$[\![\phi]\!](t, \mathbf{x}) = f(t, \mathbf{x}), \quad t > 0, \quad \mathbf{x} \in \Gamma(t), \quad (8)$$

while for conjugate mass transfer one may use Henry's law,

$$[\![\phi]\!]^{\text{He}}(t, \mathbf{x}) = f(t, \mathbf{x}), \quad t > 0, \quad \mathbf{x} \in \Gamma(t), \quad (9)$$

where $\lambda = \text{He}$ is Henry's coefficient (with $\text{He} \rightarrow 1$ when solubilities match). The right-hand side f allows for interfacial jumps associated with thin-layer effects or effective interfacial resistances.

Finally, we emphasize that the present work follows a two-fluid formulation: the bulk equations are solved separately in $\Omega^\pm(t)$ and coupled through the sharp conditions (7)-(9). This preserves phase-wise modeling flexibility and avoids the introduction of effective properties in interfacial control volumes.

3 Discrete geometric representation

The space-time formulation of the continuum model developed in Section 2 is discretized on a fixed Cartesian background grid, while the physical geometry is represented by a prescribed time-dependent interface $\Gamma(t)$. The resulting phase domains $\Omega^\pm(t)$ therefore evolve in time and continuously create and remove phase-restricted control volumes. Since the static geometric constructions, interface representations and moment-based operator assembly are described in detail in [12], we recall here only the minimal geometric notation required for the moving case and for the definition of space-time cut-cell quantities used in Section 4.

3.1 Geometrical foundations (recall)

For clarity, we present the two-dimensional setting ($d = 2$), the extension to $d = 3$ is feasible. Let $X = (x_{1/2}, x_{3/2}, \dots, x_{N+1/2})$ and $Y = (y_{1/2}, y_{3/2}, \dots, y_{M+1/2})$ be strictly increasing grid coordinates. The Cartesian cells are

$$\Omega_{i,j} = \Delta_i^1 \times \Delta_j^2, \quad \Delta_i^1 = (x_{i-1/2}, x_{i+1/2}), \quad \Delta_j^2 = (y_{j-1/2}, y_{j+1/2}),$$

for $(i, j) \in [1 \dots N] \times [1 \dots M]$. At any time t , the phase-restricted cells and the local interface segment are defined by

$$\Omega_{i,j}^\pm(t) = \Omega_{i,j} \cap \Omega^\pm(t), \quad \Gamma_{i,j}(t) = \Omega_{i,j} \cap \Gamma(t), \quad (10)$$

so that (by construction) the disjoint decomposition holds:

$$\Omega_{i,j} = \Omega_{i,j}^-(t) \cup \Gamma_{i,j}(t) \cup \Omega_{i,j}^+(t). \quad (11)$$

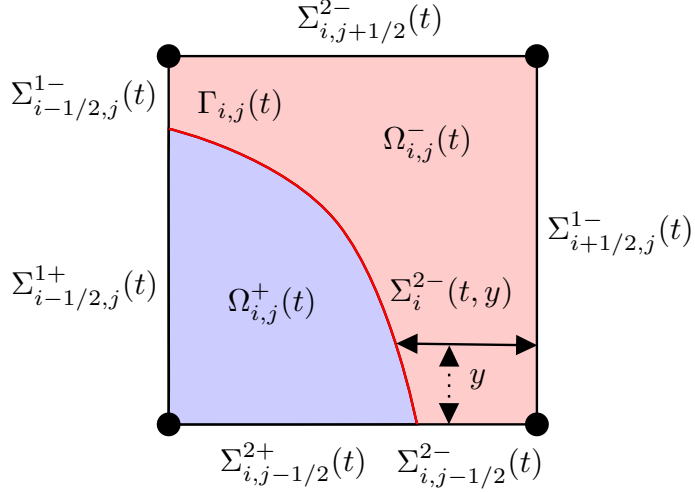


Figure 2: Geometry definitions for a moving embedded interface on a Cartesian cell. (12).

A cell is said to be *pure* in phase \pm at time t if $\Omega_{i,j}^\pm(t) = \Omega_{i,j}(t)$ and *mixed* if $\Gamma_{i,j}(t) \neq \emptyset$. In the moving setting, these labels may change with time.

Intersections of Cartesian faces with $\Omega^\pm(t)$ are denoted similarly. For example, the phase-restricted vertical and horizontal faces are

$$\Sigma_{i-1/2,j}^{1\pm}(t) = (\{x_{i-1/2}\} \times \Delta_j^2) \cap \Omega^\pm(t), \quad \Sigma_{i,j-1/2}^{2\pm}(t) = (\Delta_i^1 \times \{y_{j-1/2}\}) \cap \Omega^\pm(t),$$

with analogous definitions for the opposite faces.

These subsets induce the standard partition of the phase boundary (vertices excluded),

$$\partial\Omega_{i,j}^\pm(t) = \Gamma_{i,j}(t) \cup \Sigma_{i-1/2,j}^{1\pm}(t) \cup \Sigma_{i+1/2,j}^{1\pm}(t) \cup \Sigma_{i,j-1/2}^{2\pm}(t) \cup \Sigma_{i,j+1/2}^{2\pm}(t), \quad (12)$$

which is the starting point for the discrete flux balances.

We also recall

$$\begin{aligned} \Sigma_j^{1\pm}(t, x) &:= (\{x\} \times \Delta_j^2) \cap \Omega^\pm(t), & \Sigma_i^{2\pm}(t, y) &:= (\Delta_i^1 \times \{y\}) \cap \Omega^\pm(t), \\ \Omega_j^{1\pm}(t, \Delta) &:= (\Delta \times \Delta_j^2) \cap \Omega^\pm(t), & \Omega_i^{2\pm}(t, \Delta) &:= (\Delta_i^1 \times \Delta) \cap \Omega^\pm(t). \end{aligned}$$

Finally, we introduce a strictly increasing sequence of time instants

$$0 = t_0 < t_1 < \dots < t_n < \dots,$$

and denote $\Delta t_n := t_{n+1} - t_n$.

3.2 Reduced geometric description

As in the companion static paper, all discrete operators are expressed using a reduced set of geometric moments. For any measurable set $\Xi \subset \mathbb{R}^d$ and any integrable function f (typically a monomial), we use the shorthand notation

$$\langle \Xi, f \rangle := \int_{\mathbf{x} \in \Xi} f(\mathbf{x}) d\mathbf{x}. \quad (13)$$

This notation is employed to define phase-restricted cell volumes, face apertures and first moments over the time-dependent sets $\Omega_{i,j}^\pm(t)$ and $\Sigma^{k\pm}(t)$, from which centroids and auxiliary moments are derived.

For completeness, we recall the spatial low-order moments used by the static operators (see the companion paper for the full discussion and computation). On the Cartesian cell $\Omega_{i,j}$, the cell volume is

$$V_{i,j} := \langle \Omega_{i,j}, 1 \rangle = (x_{i+\frac{1}{2}} - x_{i-\frac{1}{2}})(y_{j+\frac{1}{2}} - y_{j-\frac{1}{2}}),$$

and the phase-restricted volumes (time-dependent in the moving setting) are

$$V_{i,j}^\pm(t) := \langle \Omega_{i,j}^\pm(t), 1 \rangle. \quad (14)$$

The cell center coordinates are

$$x_i := \frac{\langle \Omega_{i,j}, x \rangle}{\langle \Omega_{i,j}, 1 \rangle} = \frac{x_{i-\frac{1}{2}} + x_{i+\frac{1}{2}}}{2}, \quad y_j := \frac{\langle \Omega_{i,j}, y \rangle}{\langle \Omega_{i,j}, 1 \rangle} = \frac{y_{j-\frac{1}{2}} + y_{j+\frac{1}{2}}}{2},$$

and the phase centroids are defined by

$$x_{i,j}^\pm(t) := \begin{cases} \langle \Omega_{i,j}^\pm(t), x \rangle / V_{i,j}^\pm(t), & \text{if } V_{i,j}^\pm(t) \neq 0, \\ x_i, & \text{otherwise,} \end{cases} \quad y_{i,j}^\pm(t) := \begin{cases} \langle \Omega_{i,j}^\pm(t), y \rangle / V_{i,j}^\pm(t), & \text{if } V_{i,j}^\pm(t) \neq 0, \\ y_j, & \text{otherwise.} \end{cases} \quad (15)$$

The phase-restricted face apertures are

$$A_{i-\frac{1}{2},j}^{1\pm}(t) := \langle \Sigma_{i-\frac{1}{2},j}^{1\pm}(t), 1 \rangle, \quad A_{i,j-\frac{1}{2}}^{2\pm}(t) := \langle \Sigma_{i,j-\frac{1}{2}}^{2\pm}(t), 1 \rangle. \quad (16)$$

When needed by the discrete operators, we also use the “second kind” spatial moments (defined from the centroids above)

$$B_{i,j}^{1\pm}(t) := \langle \Sigma_j^{1\pm}(t, x_{i,j}^\pm(t)), 1 \rangle, \quad B_{i,j}^{2\pm}(t) := \langle \Sigma_i^{2\pm}(t, y_{i,j}^\pm(t)), 1 \rangle, \quad (17)$$

and the face-centered phase volumes

$$W_{i-\frac{1}{2},j}^{1\pm}(t) := \langle \Omega_j^{1\pm}(t, x_{i-1,j}^\pm(t), x_{i,j}^\pm(t)), 1 \rangle, \quad W_{i,j-\frac{1}{2}}^{2\pm}(t) := \langle \Omega_i^{2\pm}(t, y_{i,j-1}^\pm(t), y_{i,j}^\pm(t)), 1 \rangle. \quad (18)$$

The moving-geometry extension requires that the same geometric information be integrated in time over each time slab. This is the direct consequence of applying Reynolds’ transport theorem to control volumes that evolve through $\Gamma(t)$: conservation laws over $[t_n, t_{n+1}]$ involve space-time fluxes, which naturally introduce time-integrated measures. Accordingly, we denote space-time (time-integrated) moments by calligraphic letters. For any time-dependent quantity $M(t)$ defined from spatial moments, we set

$$\mathcal{M}_{n+\frac{1}{2}} := \int_{t_n}^{t_{n+1}} M(t) dt. \quad (19)$$

In particular, the time-integrated phase volumes and face apertures are

$$\mathcal{V}_{n+\frac{1}{2},i,j}^\pm := \int_{t_n}^{t_{n+1}} V_{i,j}^\pm(t) dt = \langle [t_n, t_{n+1}], V_{i,j}^\pm(t) \rangle, \quad (20)$$

$$\mathcal{A}_{n+\frac{1}{2},i-\frac{1}{2},j}^{1\pm} := \int_{t_n}^{t_{n+1}} A_{i-\frac{1}{2},j}^{1\pm}(t) dt = \langle [t_n, t_{n+1}], A_{i-\frac{1}{2},j}^{1\pm}(t) \rangle, \quad (21)$$

$$\mathcal{A}_{n+\frac{1}{2},i,j-\frac{1}{2}}^{2\pm} := \int_{t_n}^{t_{n+1}} A_{i,j-\frac{1}{2}}^{2\pm}(t) dt = \langle [t_n, t_{n+1}], A_{i,j-\frac{1}{2}}^{2\pm}(t) \rangle. \quad (22)$$

with analogous definitions for the other Cartesian faces. These extensive quantities satisfy $[\mathcal{V}] = m^d$ s and $[\mathcal{A}] = m^{d-1}$ s.

Time-integrated centroids are defined from normalized first moments. In $d = 2$,

$$\mathcal{X}_{n+\frac{1}{2},i,j}^\pm := \begin{cases} \frac{\int_{t_n}^{t_{n+1}} \langle \Omega_{i,j}^\pm(t), x \rangle dt}{\mathcal{V}_{n+\frac{1}{2},i,j}^\pm}, & \text{if } \mathcal{V}_{n+\frac{1}{2},i,j}^\pm \neq 0, \\ x_i, & \text{otherwise,} \end{cases} \quad (23)$$

$$\mathcal{Y}_{n+\frac{1}{2},i,j}^\pm := \begin{cases} \frac{\int_{t_n}^{t_{n+1}} \langle \Omega_{i,j}^\pm(t), y \rangle dt}{\mathcal{V}_{n+\frac{1}{2},i,j}^\pm}, & \text{if } \mathcal{V}_{n+\frac{1}{2},i,j}^\pm \neq 0, \\ y_j, & \text{otherwise.} \end{cases} \quad (24)$$

These remain intensive, i.e. $[\mathcal{X}] = [\mathcal{Y}] = m$.

The discrete operators further require time-integrated auxiliary measures (the “moments of the second kind”) that are the direct time-integrated counterparts of the static quantities introduced in the

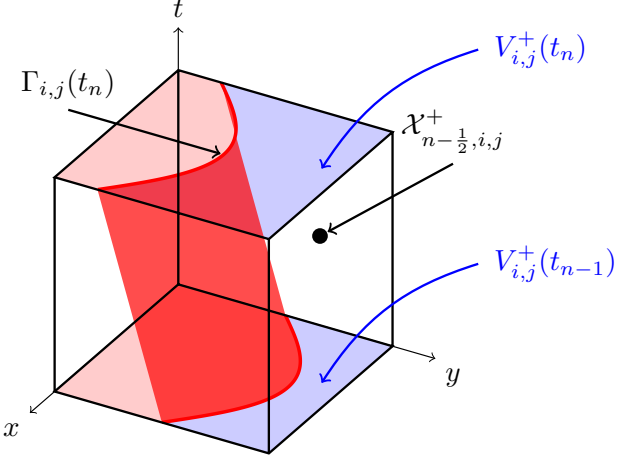


Figure 3: Space-time control volume over $[t_n, t_{n+1}]$ illustrating the phase-restricted sub-volumes $V_{i,j}^+(t_n)$ and $V_{i,j}^+(t_{n+1})$ and the swept interface within the time slab.

companion paper. Using the space-time centroids above, we define

$$\mathcal{B}_{n+\frac{1}{2},i,j}^{1\pm} := \int_{t_n}^{t_{n+1}} \left\langle \Sigma_j^{1\pm} \left(t, \mathcal{X}_{n+\frac{1}{2},i,j}^\pm \right), 1 \right\rangle dt, \quad \mathcal{B}_{n+\frac{1}{2},i,j}^{2\pm} := \int_{t_n}^{t_{n+1}} \left\langle \Sigma_i^{2\pm} \left(t, \mathcal{Y}_{n+\frac{1}{2},i,j}^\pm \right), 1 \right\rangle dt, \quad (25)$$

$$\mathcal{W}_{n+\frac{1}{2},i-\frac{1}{2},j}^{1\pm} := \int_{t_n}^{t_{n+1}} \left\langle \left((\mathcal{X}_{n+\frac{1}{2},i-1,j}^\pm, \mathcal{X}_{n+\frac{1}{2},i,j}^\pm) \times (y_{j-\frac{1}{2}}, y_{j+\frac{1}{2}}) \right) \cap \Omega^\pm(t), 1 \right\rangle dt, \quad (26)$$

$$\mathcal{W}_{n+\frac{1}{2},i,j-\frac{1}{2}}^{2\pm} := \int_{t_n}^{t_{n+1}} \left\langle \left((x_{i-\frac{1}{2}}, x_{i+\frac{1}{2}}) \times (\mathcal{Y}_{n+\frac{1}{2},i,j-1}^\pm, \mathcal{Y}_{n+\frac{1}{2},i,j}^\pm) \right) \cap \Omega^\pm(t), 1 \right\rangle dt. \quad (27)$$

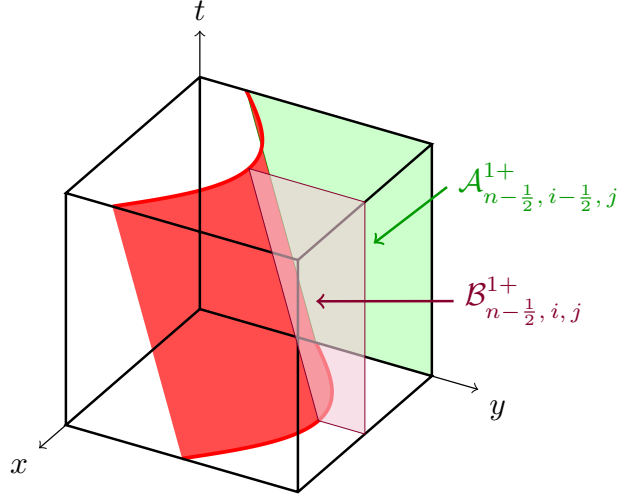


Figure 4: Space-time cell highlighting a time-integrated face aperture $\mathcal{A}_{n+\frac{1}{2},i-\frac{1}{2},j}^{1+}$ and an auxiliary measure of the second kind $\mathcal{B}_{n+\frac{1}{2},i,j}^{1+}$ used by the discrete operators.

These definitions mirror the static construction; the only change is the integration in time over the evolving phase domains. The resulting set $\{\mathcal{V}, \mathcal{A}, \mathcal{X}, \mathcal{Y}, \mathcal{B}, \mathcal{W}\}$ provides all geometric moments required by the space-time discrete operators and remains well-defined even in the presence of fresh/dead cut cells within the time slab.

Finally, we note that the calligraphic notation does not necessarily preserve the physical dimensions of the corresponding spatial quantities: extensive measures gain a factor of time (e.g. $[\mathcal{V}] = [V] \cdot s$, $[\mathcal{A}] = [A] \cdot s$), whereas intensive measures such as centroids retain their original dimension.

A table in Appendix A lists, for two spatial dimensions, the primary and secondary moments used in the discrete formulation.

4 Space-time two-phase cut-cell method for moving domains

We now extend the static cut-cell operators to prescribed moving geometries. To handle moving boundaries, we employ a space-time cut-cell formulation in which time is treated as an additional coordinate: a d -dimensional Cartesian mesh is viewed as a $(d+1)$ -dimensional space-time mesh over each slab $[t_n, t_{n+1}]$ (e.g. 1D \rightarrow 2D, 2D \rightarrow 3D and 3D \rightarrow 4D). In the remainder, we present the two-dimensional case ($d = 2$) for clarity but the construction extends directly to $d = 3$. This embedding turns each spatial cell into a space-time cut-cell, defined as the $(d+1)$ -dimensional polytope swept by the interface over one time step. Its boundary includes the spatial faces at t_n and t_{n+1} , the swept lateral faces and the swept interface.

Because the interface $\Gamma(t)$ evolves through the fixed Cartesian mesh, the phase occupancy of a given cell may change during a time slab. For robust assembly, we classify each spatial cell $\Omega_{i,j}$ by the behaviour of its phase volumes at the slab endpoints and within the slab.

Regular cells. A cell is called *regular* in phase \pm over $[t_n, t_{n+1}]$ if it remains pure in that phase for all times in the slab, i.e. $\Omega_{i,j}^\pm(t) = \Omega_{i,j}$ and $\Gamma_{i,j}(t) = \emptyset$ for all $t \in [t_n, t_{n+1}]$. In that case, the space-time control volume is the Cartesian prism $\Omega_{i,j} \times [t_n, t_{n+1}]$ and the geometric measures are obvious.

Cut cells and topology changes. A cell is said *cut* over $[t_n, t_{n+1}]$ if $\Gamma_{i,j}(t) \neq \emptyset$ for at least one $t \in [t_n, t_{n+1}]$. The corresponding phase volumes and face apertures vary in time and must be handled through the time-integrated moments \mathcal{V}^\pm , $\mathcal{A}^{\alpha\pm}$, etc. We further distinguish:

- **Persistent cut cells:** $\Gamma_{i,j}(t_n) \neq \emptyset$ and $\Gamma_{i,j}(t_{n+1}) \neq \emptyset$ (the cell is cut at both slab endpoints).
- **Fresh cells for phase \pm :** $V_{i,j}^\pm(t_n) = 0$ and $V_{i,j}^\pm(t_{n+1}) > 0$. The phase appears in the cell during the slab.
- **Dead cells for phase \pm :** $V_{i,j}^\pm(t_n) > 0$ and $V_{i,j}^\pm(t_{n+1}) = 0$. The phase disappears from the cell during the slab.

In all three cases, the space-time formulation provides a unique conservative update because the exchange of extensive quantities is accounted for on the complete space-time boundary (swept faces and swept interface) rather than by separate ad hoc treatments at t_n and t_{n+1} . In what follows, we construct a space-time integrated divergence operator, accounting for flux exchanges through the space-time boundary of the moving control volume, and a compatible space-time gradient operator used to approximate diffusive fluxes while preserving discrete consistency and the geometric conservation law.

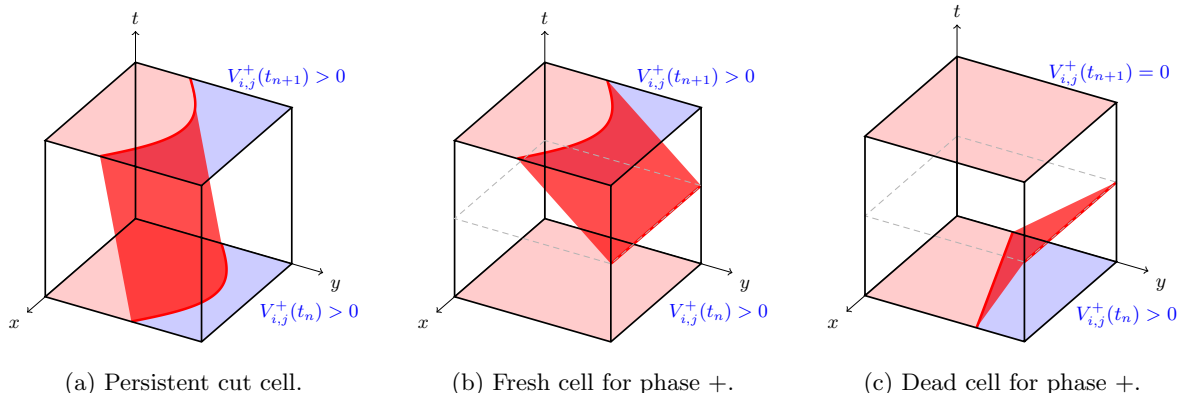


Figure 5: Space-time cut-cell taxonomy over one slab $[t_n, t_{n+1}]$: persistent cut cell (interface intersects the cell at both slab endpoints), fresh cell for phase $+$ (the $+$ phase appears during the slab) and dead cell for phase $+$ (the $+$ phase disappears during the slab).

For each active phase cell, we define the space-time averaged bulk quantity

$$\tilde{\Phi}_{n+1/2,i,j}^{\omega\pm} := \frac{\langle [t_n, t_{n+1}], \langle \Omega_{i,j}^{\pm}(t), \phi^{\pm}(t) \rangle \rangle}{\mathcal{V}_{n+1/2,i,j}^{\pm}} \quad \text{where } \mathcal{V}_{n+1/2,i,j}^{\pm} \neq 0, \quad (28)$$

The discrete (time-slab endpoint) bulk unknowns remain those of the static formulation,

$$\Phi_{n,i,j}^{\omega\pm} := \Phi_{i,j}^{\omega\pm}(t_n). \quad (29)$$

where we recall the definition of the spatial bulk average

$$\Phi_{i,j}^{\omega\pm}(t) := \langle \Omega_{i,j}^{\pm}, \phi^{\pm}(t) \rangle / V_{i,j}^{\pm} \quad \text{where } V_{i,j}^{\pm} \neq 0,$$

On interfacial (mixed) cells, we similarly introduce space-time averaged interfacial traces, defined separately on each side of $\Gamma(t)$,

$$\Phi_{n+1/2,i,j}^{\gamma\pm} := \frac{\int_{t_n}^{t_{n+1}} \langle \Gamma_{i,j}(t), \phi^{\pm}(t) \rangle dt}{\int_{t_n}^{t_{n+1}} \int_{\Gamma_{i,j}(t)} 1 dS dt}. \quad (30)$$

These interfacial quantities enter only through the same two-fluid coupling laws as in the static case.

To ensure that these discrete events are detected and treated within a single time step, we enforce an interface CFL-like constraint: the interface must not cross more than one cell in the normal direction during one update. This restriction prevents “skipped” fresh/dead transitions and guarantees that the time-integrated moments $\mathcal{V}_{n+1/2,i,j}^{\pm}$ and $\mathcal{A}_{n+1/2,i,j}^{\alpha\pm}$ capture all topological changes occurring in the slab.

4.1 Semi-discrete and discrete bulk equation

The starting point is Reynolds’ transport theorem applied to the time-evolving phase cell $\Omega_{i,j}^{\pm}(t)$,

$$\frac{d}{dt} \langle \Omega_{i,j}^{\pm}(t), C^{\pm} \phi^{\pm} \rangle = \langle \Omega_{i,j}^{\pm}(t), \partial_t(C^{\pm} \phi^{\pm}) \rangle + \int_{\partial\Omega_{i,j}^{\pm}(t)} C^{\pm} \phi^{\pm} u^{\pm} dS, \quad (31)$$

where u^{\pm} denotes the normal velocity of the moving boundary element. By definition of $\Omega_{i,j}^{\pm}(t)$, the only moving part of $\partial\Omega_{i,j}^{\pm}(t)$ is the interface segment $\Gamma_{i,j}(t)$. Cartesian cell faces are fixed. With the choice $\mathbf{n} = \mathbf{n}^-$ (red phase reference), this yields

$$u^{\pm} = \begin{cases} \mp w, & \text{on } \Gamma_{i,j}(t), \\ 0, & \text{otherwise,} \end{cases}$$

Using the bulk balance equation (4), the divergence theorem, we obtain the exact semi-discrete balance

$$C^{\pm} \frac{d}{dt} [V_{i,j}^{\pm}(t) \Phi_{i,j}^{\omega\pm}(t)] + \int_{\partial\Omega_{i,j}^{\pm}(t)} \mathbf{q}^{\pm}(t) \cdot d\mathbf{S} \mp \int_{\Gamma_{i,j}(t)} C^{\pm} \phi^{\pm}(t) w dS = \langle \Omega_{i,j}^{\pm}(t), r^{\pm}(t) \rangle, \quad (32)$$

For convenience, we introduce the phase source average

$$R_{i,j}^{\pm}(t) := \frac{\langle \Omega_{i,j}^{\pm}(t), r^{\pm}(t) \rangle}{V_{i,j}^{\pm}(t)} \quad \text{when } V_{i,j}^{\pm}(t) \neq 0.$$

Integrating (32) over the time slab $[t_n, t_{n+1}]$ gives the (space-time) fully discrete bulk equation:

$$C^{\pm} \left(V_{n+1,i,j}^{\pm} \Phi_{n+1,i,j}^{\omega\pm} - V_{n,i,j}^{\pm} \Phi_{n,i,j}^{\omega\pm} \right) + \int_{t_n}^{t_{n+1}} \int_{\partial\Omega_{i,j}^{\pm}(t)} \mathbf{q}^{\pm}(t) \cdot d\mathbf{S} dt \mp \int_{t_n}^{t_{n+1}} \int_{\Gamma_{i,j}(t)} C^{\pm} \phi^{\pm}(t) w dS dt = \mathcal{V}_{n+1/2,i,j}^{\pm} \mathcal{R}_{n+1/2,i,j}^{\pm}, \quad (33)$$

with the space-time source average

$$\mathcal{R}_{n+1/2,i,j}^{\pm} := \frac{\int_{t_n}^{t_{n+1}} \langle \Omega_{i,j}^{\pm}(t), r^{\pm}(t) \rangle dt}{\mathcal{V}_{n+1/2,i,j}^{\pm}} \quad \text{when } \mathcal{V}_{n+1/2,i,j}^{\pm} \neq 0.$$

4.1.1 Space-time-integrated divergence operator

As in the static case, the time-integrated boundary flux in (33) is split into contributions through Cartesian faces (exchange with neighboring control volumes in the same phase) and through the interface:

$$\int_{t_n}^{t_{n+1}} \int_{\partial\Omega_{i,j}^\pm(t)} \mathbf{q}^\pm \cdot d\mathbf{S} dt = \int_{t_n}^{t_{n+1}} \int_{\partial\Omega_{i,j}^\pm(t) \setminus \Gamma_{i,j}(t)} \mathbf{q}^\pm \cdot d\mathbf{S} dt + \int_{t_n}^{t_{n+1}} \int_{\Gamma_{i,j}(t)} \mathbf{q}^\pm \cdot d\mathbf{S} dt. \quad (34)$$

Both contributions are discretized using the same volume-integrated divergence operators as in the static formulation, the only change being that the geometric inputs are now time-integrated:

$$\sum_{\alpha=1}^d \mathcal{V}_{n+\frac{1}{2},i,j}^\pm \operatorname{div}_{i,j}^{\alpha\omega} \left(\mathcal{A}_{n+\frac{1}{2}}^{\alpha\pm}, \mathcal{Q}_{n+\frac{1}{2}}^{\alpha\pm} \right) \quad \text{and} \quad \sum_{\alpha=1}^d \mathcal{V}_{n+\frac{1}{2},i,j}^\pm \operatorname{div}_{i,j}^{\alpha\gamma} \left(\mathcal{A}_{n+\frac{1}{2}}^{\alpha\pm}, \mathcal{B}_{n+\frac{1}{2}}^{\alpha\pm}, \mathcal{Q}_{n+\frac{1}{2}}^{\alpha\pm} \right),$$

for the Cartesian-face and interface parts, respectively.

Accordingly, we define the time-integrated diffusive fluxes by space-time averaging over the corresponding time-dependent phase-restricted faces. In 2D, the x - and y -fluxes are

$$\mathcal{Q}_{n+\frac{1}{2},i+\frac{1}{2},j}^{1\pm} \simeq \frac{\int_{t_n}^{t_{n+1}} \left\langle \Sigma_{i+\frac{1}{2},j}^{1\pm}(t), q^{1\pm}(t) \right\rangle dt}{\mathcal{A}_{n+\frac{1}{2},i+\frac{1}{2},j}^{1\pm}}, \quad \text{when } \mathcal{A}_{n+\frac{1}{2},i+\frac{1}{2},j}^{1\pm} \neq 0, \quad (35)$$

$$\mathcal{Q}_{n+\frac{1}{2},i,j+\frac{1}{2}}^{2\pm} \simeq \frac{\int_{t_n}^{t_{n+1}} \left\langle \Sigma_{i,j+\frac{1}{2}}^{2\pm}(t), q^{2\pm}(t) \right\rangle dt}{\mathcal{A}_{n+\frac{1}{2},i,j+\frac{1}{2}}^{2\pm}}, \quad \text{when } \mathcal{A}_{n+\frac{1}{2},i,j+\frac{1}{2}}^{2\pm} \neq 0, \quad (36)$$

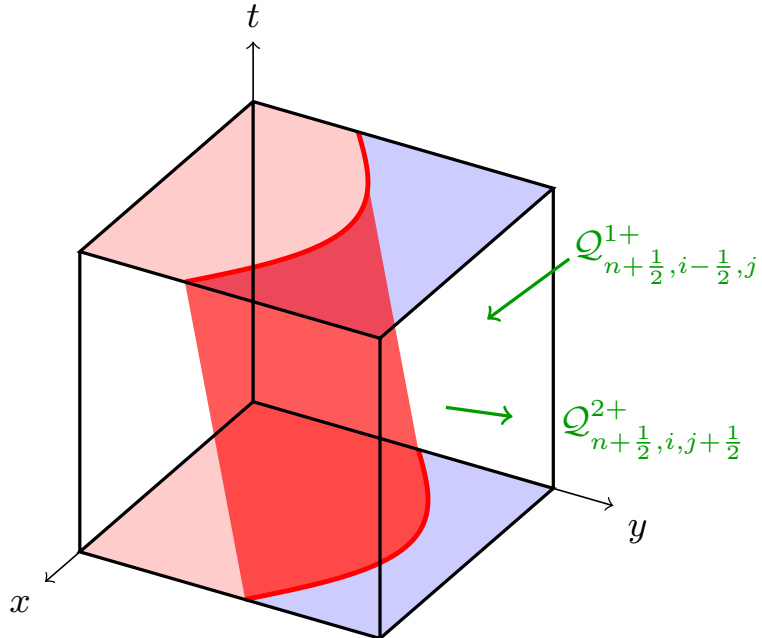


Figure 6: Space-time cut-cell representation of the time-integrated diffusive fluxes through Cartesian faces over one slab $[t_n, t_{n+1}]$. Only two fluxes are shown for clarity: the x -face flux $\mathcal{Q}_{n+\frac{1}{2}, i-\frac{1}{2}, j}^{1+}$ and the y -face flux $\mathcal{Q}_{n+\frac{1}{2}, i, j+\frac{1}{2}}^{2+}$, defined as space-time averages over the corresponding phase-restricted swept faces.

4.1.2 Geometric conservation law

A fundamental requirement of moving-boundary finite-volume schemes is the exact preservation of constant states. Consider the particular case where C^\pm and ϕ^\pm are constants, so that $\mathbf{q}^\pm \equiv \mathbf{0}$ and $r^\pm \equiv 0$.

The bulk balance (4) then reduces to the identity $0 = 0$ but integrating it over the evolving phase cell $\Omega_{i,j}^\pm(t)$ over one time slab yields the purely geometric relation

$$V_{n+1,i,j}^\pm - V_{n,i,j}^\pm \mp \int_{t_n}^{t_{n+1}} \int_{\Gamma_{i,j}(t)} w \, dS \, dt = 0, \quad (37)$$

which is the geometric conservation law (GCL) in the present cut-cell setting. A discrete scheme that satisfies (37) reproduces constant solutions exactly and prevents spurious source terms induced solely by geometric motion [5].

To approximate the interfacial sweeping term in (33), we apply the space-time quadrature consistent with the definition of the interfacial trace (30):

$$\int_{t_n}^{t_{n+1}} \int_{\Gamma_{i,j}(t)} C^\pm \phi^\pm(t) w \, dS \, dt \simeq C^\pm \Phi_{n+\frac{1}{2},i,j}^{\gamma\pm} \int_{t_n}^{t_{n+1}} \int_{\Gamma_{i,j}(t)} w \, dS \, dt.$$

Using the GCL (37), this becomes

$$\int_{t_n}^{t_{n+1}} \int_{\Gamma_{i,j}(t)} C^\pm \phi^\pm(t) w \, dS \, dt \simeq \mp C^\pm \Phi_{n+\frac{1}{2},i,j}^{\gamma\pm} (V_{n+1,i,j}^\pm - V_{n,i,j}^\pm). \quad (38)$$

Substituting (38) together with the space-time-integrated divergence discretization of Section 4.1.1 into (33) yields the discrete bulk balance in conservative space-time form:

$$\begin{aligned} & C^\pm (V_{n+1,i,j}^\pm \Phi_{n+1,i,j}^{\omega\pm} - V_{n,i,j}^\pm \Phi_{n,i,j}^{\omega\pm}) \\ & + \sum_{\alpha=1}^d [\mathcal{V}_{n+\frac{1}{2},i,j}^\pm \operatorname{div}_{i,j}^{\alpha\omega} (\mathcal{A}_{n+\frac{1}{2}}^{\alpha\pm}, \mathcal{Q}_{n+\frac{1}{2}}^{\alpha\pm}) + \mathcal{V}_{n+\frac{1}{2},i,j}^\pm \operatorname{div}_{i,j}^{\alpha\gamma} (\mathcal{A}_{n+\frac{1}{2}}^{\alpha\pm}, \mathcal{B}_{n+\frac{1}{2}}^{\alpha\pm}, \mathcal{Q}_{n+\frac{1}{2}}^{\alpha\pm})] \\ & + C^\pm \Phi_{n+\frac{1}{2},i,j}^{\gamma\pm} (V_{n+1,i,j}^\pm - V_{n,i,j}^\pm) = \mathcal{V}_{n+\frac{1}{2},i,j}^\pm \mathcal{R}_{n+\frac{1}{2},i,j}^\pm. \end{aligned} \quad (39)$$

Equation (39) reduces to the static cut-cell balance when the geometry is fixed (all time-integrated measures reduce to $\mathcal{A} = \Delta t_n A$, $\mathcal{V} = \Delta t_n V$ and the volume difference vanishes).

4.1.3 Space-time-integrated gradient operator

The construction of the diffusive fluxes in (39) follows the same principles as in the static formulation but with space-time geometric weights. In particular, the constitutive law $\mathbf{q}^\pm = -K^\pm \nabla \phi^\pm$ requires a discrete gradient operator that is compatible with the space-time divergence operators.

We therefore define the space-time gradient operator by reusing the static bulk and interfacial gradient components, replacing (A, B, W) by their time-integrated counterparts $(\mathcal{A}, \mathcal{B}, \mathcal{W})$ and using the space-time averaged unknowns $\tilde{\Phi}^{\omega\pm}$ and $\Phi_{n+\frac{1}{2}}^{\gamma\pm}$:

$$\operatorname{grad}_{i-\frac{1}{2},j}^{1\omega} (\mathcal{B}_{n+\frac{1}{2}}^{1\pm}, \mathcal{W}_{n+\frac{1}{2}}^{1\pm}, \tilde{\Phi}_{n+\frac{1}{2}}^{\omega\pm}), \quad \operatorname{grad}_{i-\frac{1}{2},j}^{1\gamma} (\mathcal{A}_{n+\frac{1}{2}}^{1\pm}, \mathcal{B}_{n+\frac{1}{2}}^{1\pm}, \mathcal{W}_{n+\frac{1}{2}}^{1\pm}, \Phi_{n+\frac{1}{2}}^{\gamma\pm}),$$

with analogous expressions in the other coordinate directions. The space-time diffusive flux through an x -oriented face then reads

$$\mathcal{Q}_{n+\frac{1}{2},i-\frac{1}{2},j}^{1\pm} = -K^\pm \left[\operatorname{grad}_{i-\frac{1}{2},j}^{1\omega} (\mathcal{B}_{n+\frac{1}{2}}^{1\pm}, \mathcal{W}_{n+\frac{1}{2}}^{1\pm}, \tilde{\Phi}_{n+\frac{1}{2}}^{\omega\pm}) + \operatorname{grad}_{i-\frac{1}{2},j}^{1\gamma} (\mathcal{A}_{n+\frac{1}{2}}^{1\pm}, \mathcal{B}_{n+\frac{1}{2}}^{1\pm}, \mathcal{W}_{n+\frac{1}{2}}^{1\pm}, \Phi_{n+\frac{1}{2}}^{\gamma\pm}) \right], \quad (40)$$

and similarly for $\mathcal{Q}_{n+\frac{1}{2},i,j-\frac{1}{2}}^{2\pm}$ in the y direction. This construction reduces exactly to the static one when the geometry is fixed and provides a space-time consistent approximation of the diffusive term in (39).

4.1.4 Fresh and dead cells: topology change

The fully discrete space-time balances (39)-(40) apply directly to regular cells and persistent cut cells, i.e. configurations for which both endpoint phase volumes are nonzero, $V_{n,i,j}^\pm > 0$ and $V_{n+1,i,j}^\pm > 0$. In that case, the space-time bulk state used by the constitutive law is closed by the standard θ -scheme between t_n and t_{n+1} .

When the interface motion creates or removes a phase within a cell during the slab, i.e. for fresh or dead cut cells, the space-time flux evaluation still requires a well-defined slab state $\tilde{\Phi}_{n+\frac{1}{2},i,j}^{\omega\pm}$ even though one of the endpoint unknowns is absent. We therefore adopt the following state-dependent closure:

$$\tilde{\Phi}_{n+\frac{1}{2},i,j}^{\omega\pm} = \begin{cases} \Phi_{n+1,i,j}^{\omega\pm}, & V_{n,i,j}^{\pm} = 0, V_{n+1,i,j}^{\pm} > 0 \quad (\text{fresh cell}), \\ \Phi_{\text{loc},i,j}^{\omega\pm}, & V_{n,i,j}^{\pm} > 0, V_{n+1,i,j}^{\pm} = 0 \quad (\text{dead cell}), \\ (1 - \theta) \Phi_{n,i,j}^{\omega\pm} + \theta \Phi_{n+1,i,j}^{\omega\pm}, & V_{n,i,j}^{\pm} > 0, V_{n+1,i,j}^{\pm} > 0 \quad (\text{persistent/regular cell}). \end{cases} \quad (41)$$

In persistent/regular cells, (41) reduces to the usual time interpolation and is passed to the space-time gradient operator in the constitutive relation (40). In transitioning cells, it provides a consistent slab state so that the face fluxes remain well defined and global conservation over $[t_n, t_{n+1}]$ is preserved.

Dead cells. For dead cells ($V_{n+1,i,j}^{\pm} = 0$), no bulk unknown is advanced at t_{n+1} because the phase becomes inactive in $\Omega_{i,j}$. The closure value $\Phi_{\text{loc},i,j}^{\omega\pm}$ is therefore computed locally by enforcing that the space-time balance (39) holds on the disappearing control volume, with all face fluxes assembled using $\tilde{\Phi}^{\omega\pm}$ and the space-time geometry:

$$\begin{aligned} - C^{\pm} V_{n,i,j}^{\pm} \Phi_{n,i,j}^{\omega\pm} + \sum_{\alpha=1}^d \left[\mathcal{V}_{n+\frac{1}{2},i,j}^{\pm} \text{div}_{i,j}^{\alpha\omega} \left(\mathcal{A}_{n+\frac{1}{2}}^{\alpha\pm}, \mathcal{Q}_{n+\frac{1}{2}}^{\alpha\pm}(\tilde{\Phi}^{\omega\pm}) \right) \right. \\ \left. + \mathcal{V}_{n+\frac{1}{2},i,j}^{\pm} \text{div}_{i,j}^{\alpha\gamma} \left(\mathcal{A}_{n+\frac{1}{2}}^{\alpha\pm}, \mathcal{B}_{n+\frac{1}{2}}^{\alpha\pm}, \mathcal{Q}_{n+\frac{1}{2}}^{\alpha\pm}(\tilde{\Phi}^{\omega\pm}) \right) \right] \\ - C^{\pm} \Phi_{n+\frac{1}{2},i,j}^{\gamma\pm} V_{n,i,j}^{\pm} = \mathcal{V}_{n+\frac{1}{2},i,j}^{\pm} \mathcal{R}_{n+\frac{1}{2},i,j}^{\pm}. \end{aligned} \quad (42)$$

Since $V_{n+1,i,j}^{\pm} = 0$, (42) yields a single scalar linear constraint for $\Phi_{\text{loc},i,j}^{\omega\pm}$ because the fluxes $\mathcal{Q}_{n+\frac{1}{2}}^{\alpha\pm}$ depend linearly on the slab states through (40). In practice, (42) is assembled as

$$a_{i,j}^{\pm} \Phi_{\text{loc},i,j}^{\omega\pm} = b_{i,j}^{\pm},$$

where $a_{i,j}^{\pm}$ and $b_{i,j}^{\pm}$ gather, respectively, the coefficients and known terms produced by the (linear) divergence-gradient-constitutive composition when only the local dead-cell state is left unknown. The resulting $\Phi_{\text{loc},i,j}^{\omega\pm}$ is used only to evaluate fluxes in the current slab and is not carried to the next time level.

Fresh cells. For newly created cells ($V_{n,i,j}^{\pm} = 0, V_{n+1,i,j}^{\pm} > 0$), we set (41) with $\tilde{\Phi}_{n+\frac{1}{2},i,j}^{\omega\pm} = \Phi_{n+1,i,j}^{\omega\pm}$. The slab balance then specializes to

$$\begin{aligned} C^{\pm} V_{n+1,i,j}^{\pm} \Phi_{n+1,i,j}^{\omega\pm} + \sum_{\alpha=1}^d \left[\mathcal{V}_{n+\frac{1}{2},i,j}^{\pm} \text{div}_{i,j}^{\alpha\omega} \left(\mathcal{A}_{n+\frac{1}{2}}^{\alpha\pm}, \mathcal{Q}_{n+\frac{1}{2}}^{\alpha\pm}(\tilde{\Phi}^{\omega\pm}) \right) \right. \\ \left. + \mathcal{V}_{n+\frac{1}{2},i,j}^{\pm} \text{div}_{i,j}^{\alpha\gamma} \left(\mathcal{A}_{n+\frac{1}{2}}^{\alpha\pm}, \mathcal{B}_{n+\frac{1}{2}}^{\alpha\pm}, \mathcal{Q}_{n+\frac{1}{2}}^{\alpha\pm}(\tilde{\Phi}^{\omega\pm}) \right) \right] \\ - C^{\pm} \Phi_{n+\frac{1}{2},i,j}^{\gamma\pm} V_{n+1,i,j}^{\pm} = \mathcal{V}_{n+\frac{1}{2},i,j}^{\pm} \mathcal{R}_{n+\frac{1}{2},i,j}^{\pm}, \end{aligned} \quad (43)$$

so no additional local unknown is introduced: fluxes entering the fresh cell are computed using the initialized slab state, which activates the new control volume consistently.

Summing the discrete balances over all cells (regular, persistent, fresh and dead) and adding the discrete interface balance of Section 4.2 cancels all internal face contributions, leaving only volumetric sources. Global conservation is therefore maintained across topology changes.

4.2 Space-time interface balance

The interface equations are discretized as in the static formulation but the space-time setting introduces the additional sweeping contribution associated with interface motion. On each interfacial segment $\Gamma_{i,j}(t)$, the instantaneous surface balance (7) reads

$$[\![\mathbf{q} \cdot \mathbf{n} - C \phi w]\!] = 0, \quad (44)$$

Integrating (44) over the slab $[t_n, t_{n+1}]$ and discretizing the resulting surface integrals using the space-time geometric operators yields the space-time interface balance. Using the same space-time-interfacial quadrature as in Section 4.1.2, the sweeping term can be written in terms of the phase-volume change over the slab, leading to

$$\sum_{\alpha=1}^d \left[\mathcal{V}_{n+\frac{1}{2},i,j}^+ \operatorname{div}_{i,j}^{\alpha\gamma} (\mathcal{A}_{n+\frac{1}{2}}^{\alpha+}, \mathcal{B}_{n+\frac{1}{2}}^{\alpha+}, \mathcal{Q}_{n+\frac{1}{2}}^{\alpha+}) - \mathcal{V}_{n+\frac{1}{2},i,j}^- \operatorname{div}_{i,j}^{\alpha\gamma} (\mathcal{A}_{n+\frac{1}{2}}^{\alpha-}, \mathcal{B}_{n+\frac{1}{2}}^{\alpha-}, \mathcal{Q}_{n+\frac{1}{2}}^{\alpha-}) \right] - \llbracket C \Phi_{n+\frac{1}{2},i,j}^{\gamma\pm} \rrbracket (V_{n+1,i,j}^- - V_{n,i,j}^-) = 0, \quad (45)$$

where the last term expresses the space-time sweeping flux in terms of the phase-volume variation (here written using the reference phase “-”). Equivalent expressions are obtained by using the “+” phase, since $V_{n+1,i,j}^- - V_{n,i,j}^- = -(V_{n+1,i,j}^+ - V_{n,i,j}^+)$.

The interfacial closure (continuity / Henry law / prescribed jump) is unchanged from the static case and is imposed at the same intermediate time level $t_{n+\frac{1}{2}}$:

$$\Phi_{n+\frac{1}{2},i,j}^{\gamma+} - \lambda \Phi_{n+\frac{1}{2},i,j}^{\gamma-} = \mathcal{F}_{n+\frac{1}{2},i,j}, \quad (46)$$

where \mathcal{F} denotes the space-time averaged interfacial source term.

In the particular case of planar, mesh-aligned interfaces with $w = 0$ (no sweeping), (45)-(46) reduce to the static interface relations.

4.3 Block structure of the linear system

As in the static formulation, the continuum model is linear and the fully discrete space-time equations over a slab $[t_n, t_{n+1}]$ can be written in sparse matrix-vector form. Even for $\theta = 0$ (explicit Euler), the unknowns at time level $n + 1$ remain coupled through the interfacial balance and closure. At each step, the numerical update therefore amounts to solving a sparse linear system coupling bulk and interfacial unknowns.

We eliminate the space-time diffusive fluxes $\mathcal{Q}^{\alpha\pm}$ using the constitutive closure (40), leaving the bulk and interfacial unknowns as the remaining degrees of freedom. We use the ordering

$$\mathbf{x}_{n+1} = (\Phi_{n+1}^{\omega-}, \Phi_{n+1}^{\omega+}, \Phi_{n+\frac{1}{2}}^{\gamma-}, \Phi_{n+\frac{1}{2}}^{\gamma+}).$$

We introduce diagonal mass-like matrices

$$M_{\text{st}}^{\pm} := \frac{C^{\pm}}{\Delta t_n} \operatorname{diag}(V_{n+1}^{\pm}), \quad (47)$$

In addition, the sweeping (interface-advection) contribution in (39) introduces a diagonal coupling between the bulk equations and the interfacial unknowns. We collect it into

$$A_{\text{adv}}^{\pm} := \mp C^{\pm} \operatorname{diag}(V_{n+1}^{\pm} - V_n^{\pm}), \quad (48)$$

which multiplies $\Phi_{n+\frac{1}{2}}^{\gamma\pm}$ in the bulk balance of phase \pm .

Let $\operatorname{div}^{\alpha\omega}$ and $\operatorname{div}^{\alpha\gamma}$ denote the bulk and interfacial contributions to the divergence operator used in (39) and let $\operatorname{grad}^{\alpha\omega}$ and $\operatorname{grad}^{\alpha\gamma}$ denote the corresponding gradient contributions used in (40). Eliminating $\mathcal{Q}^{\alpha\pm}$ yields space-time diffusion operators built from the space-time moments $(\mathcal{V}, \mathcal{A}, \mathcal{B}, \mathcal{W})$:

$$L_{\text{st}}^{\omega\omega, \pm} := - \sum_{\alpha} \partial_{\mathcal{Q}} \left[\mathcal{V}^{\pm} \operatorname{div}^{\alpha\omega} (\mathcal{A}_{n+\frac{1}{2}}^{\alpha\pm}, \cdot) \right] K^{\pm} \partial_{\Phi} \operatorname{grad}^{\alpha\omega} (\mathcal{B}_{n+\frac{1}{2}}^{\alpha\pm}, \mathcal{W}_{n+\frac{1}{2}}^{\alpha\pm}, \cdot), \quad (49)$$

$$L_{\text{st}}^{\omega\gamma, \pm} := - \sum_{\alpha} \partial_{\mathcal{Q}} \left[\mathcal{V}^{\pm} \operatorname{div}^{\alpha\omega} (\mathcal{A}_{n+\frac{1}{2}}^{\alpha\pm}, \cdot) \right] K^{\pm} \partial_{\Phi} \operatorname{grad}^{\alpha\gamma} (\mathcal{A}_{n+\frac{1}{2}}^{\alpha\pm}, \mathcal{B}_{n+\frac{1}{2}}^{\alpha\pm}, \mathcal{W}_{n+\frac{1}{2}}^{\alpha\pm}, \cdot), \quad (50)$$

$$L_{\text{st}}^{\gamma\omega, \pm} := - \sum_{\alpha} \partial_{\mathcal{Q}} \left[\mathcal{V}^{\pm} \operatorname{div}^{\alpha\gamma} (\mathcal{A}_{n+\frac{1}{2}}^{\alpha\pm}, \mathcal{B}_{n+\frac{1}{2}}^{\alpha\pm}, \cdot) \right] K^{\pm} \partial_{\Phi} \operatorname{grad}^{\alpha\omega} (\mathcal{B}_{n+\frac{1}{2}}^{\alpha\pm}, \mathcal{W}_{n+\frac{1}{2}}^{\alpha\pm}, \cdot), \quad (51)$$

$$L_{\text{st}}^{\gamma\gamma, \pm} := - \sum_{\alpha} \partial_{\mathcal{Q}} \left[\mathcal{V}^{\pm} \operatorname{div}^{\alpha\gamma} (\mathcal{A}_{n+\frac{1}{2}}^{\alpha\pm}, \mathcal{B}_{n+\frac{1}{2}}^{\alpha\pm}, \cdot) \right] K^{\pm} \partial_{\Phi} \operatorname{grad}^{\alpha\gamma} (\mathcal{A}_{n+\frac{1}{2}}^{\alpha\pm}, \mathcal{B}_{n+\frac{1}{2}}^{\alpha\pm}, \mathcal{W}_{n+\frac{1}{2}}^{\alpha\pm}, \cdot). \quad (52)$$

Here $\partial_{\mathcal{Q}}$ and ∂_{Φ} denote Jacobians of the divergence and gradient operators with respect to fluxes and unknowns, respectively. Since the discrete operators are linear in \mathcal{Q} and Φ , these Jacobians reduce to constant sparse matrices.

Collecting the two bulk balances, the space-time interface balance and the interfacial closure, we obtain the block system

$$\left[\begin{array}{c|c|c|c} M_{\text{st}}^- + \theta L_{\text{st}}^{\omega\omega,-} & 0 & \theta L_{\text{st}}^{\omega\gamma,-} - A_{\text{adv}}^- & 0 \\ \hline 0 & M_{\text{st}}^+ + \theta L_{\text{st}}^{\omega\omega,+} & 0 & \theta L_{\text{st}}^{\omega\gamma,+} - A_{\text{adv}}^+ \\ -\theta L_{\text{st}}^{\gamma\omega,-} & \theta L_{\text{st}}^{\gamma\omega,+} & -L_{\text{st}}^{\gamma\gamma,-} + A_{\text{adv}}^- & L_{\text{st}}^{\gamma\gamma,+} - A_{\text{adv}}^+ \\ 0 & 0 & -\lambda I & I \end{array} \right] \left[\begin{array}{c} \Phi_{n+1}^{\omega-} \\ \Phi_{n+1}^{\omega+} \\ \Phi_{n+\frac{1}{2}}^{\gamma-} \\ \Phi_{n+\frac{1}{2}}^{\gamma+} \end{array} \right] = \text{RHS}_{\text{st}}, \quad (53)$$

where RHS_{st} gathers all known contributions from the previous time level (e.g. $\Phi_n^{\omega\pm}$), space-time source terms and any prescribed interfacial forcing.

The horizontal and vertical separators highlight the same arrow-type coupling as in the static case: two decoupled bulk blocks coupled only through the interface unknowns.

In the limit of a fixed interface ($V_{n+1}^{\pm} = V_n^{\pm}$, hence $A_{\text{adv}}^{\pm} = 0$ and $\mathcal{A} \rightarrow A \Delta t_n$, $\mathcal{B} \rightarrow B \Delta t_n$, $\mathcal{W} \rightarrow W \Delta t_n$, $\mathcal{V} \rightarrow V \Delta t_n$), (53) reduces exactly to the static block formulation.

5 Numerical validation in moving domains

This section assesses the accuracy and robustness of the proposed space-time cut-cell method in the presence of prescribed moving geometries. All tests are performed on a fixed Cartesian background grid while the physical domain evolves through a sharp interface $\Gamma(t)$, continuously creating and removing cut cells within each time slab. The numerical study targets three complementary objectives: (i) verifying the correctness of the space-time geometric moments and quadratures used by the operators, including the handling of fresh/dead cells; (ii) validating the full diffusion solver on classical moving-boundary benchmarks in two and three dimensions; and (iii) demonstrating that the two-phase coupling remains accurate and conservative when the interface sweeps across the mesh.

Let $\phi^{\text{ex}}(\mathbf{x}, t)$ denote the exact solution. Errors are evaluated from cell-averaged unknowns at selected times t_n (typically the final time), and reported separately over regular cells and cut cells. The index sets are defined by

$$\mathcal{I}_{\text{reg}} = \{(i, j) : \Gamma_{i,j} = \emptyset\}, \quad \mathcal{I}_{\text{cut}} = \{(i, j) : \Gamma_{i,j} \neq \emptyset\}, \quad \mathcal{I}_{\text{all}} = \mathcal{I}_{\text{reg}} \cup \mathcal{I}_{\text{cut}}.$$

For any subset $S \in \{\text{reg}, \text{cut}, \text{all}\}$, we define the discrete L^2 error norm as

$$\|e(t_n)\|_{2,S} = \left(\frac{\sum_{(i,j) \in \mathcal{I}_S} V_{i,j} |\Phi_{n,i,j}^{\omega} - \Phi_{n,i,j}^{\text{ex}}|^2}{\sum_{(i,j) \in \mathcal{I}_S} V_{i,j}} \right)^{1/2}, \quad (54)$$

where $\phi_{n,i,j}^{\text{ex}}$ denotes the exact solution evaluated consistently with the discrete unknown e.g. at the cell centroid for cell averages. We report

$$\|e\|_{2,\text{reg}}, \quad \|e\|_{2,\text{cut}}, \quad \|e\|_{2,\text{all}}.$$

The empirical convergence order is estimated between two successive grid resolutions h_i and h_{i+1} using

$$p_{2,S} = \frac{\log(\|e\|_{2,S}^{(i)} / \|e\|_{2,S}^{(i+1)})}{\log(h_i / h_{i+1})}, \quad S \in \{\text{reg}, \text{cut}, \text{all}\}. \quad (55)$$

Several benchmarks are formulated in a single moving domain (one material region), i.e. only one phase is physically present. In our two-fluid framework, this is recovered by selecting a single active phase (say $\Omega^-(t)$) and treating the complement as inactive. The interface $\Gamma(t)$ then acts as a prescribed moving boundary of $\Omega^-(t)$ and the discrete update reduces to the single-phase counterpart of (39)-(40) without interfacial coupling unknowns. Concretely, the continuity/Henry closure and the space-time interface balance are dropped and boundary conditions are imposed directly on $\Gamma(t)$ (Dirichlet/Neumann/Robin), while the space-time sweeping term and the geometric conservation law remain active and ensure exact preservation during the motion.

5.1 4D geometric integration: validation of the space-time moment integration engine

A central ingredient of the space-time formulation is the accurate evaluation of time-integrated geometric moments over a slab $[t_n, t_{n+1}]$. In three spatial dimensions, these moments correspond to four-dimensional measures in (x, y, z, t) and their computation requires robust clipping and integration of $(d+1)$ -dimensional polytopes. To validate this component independently of the PDE discretization, we perform a purely geometric test in \mathbb{R}^4 .

We consider a uniform Cartesian grid on a fixed four-dimensional box $\Omega_4 \subset \mathbb{R}^4$ with N cells per direction and mesh size $h = 1/N$. For each test geometry, defined by a smooth level-set $\Psi(\mathbf{x})$ in \mathbb{R}^4 , we compute the hypervolume of the restricted set $\{\Psi < 0\} \cap \Omega_4$. The geometric quantities are evaluated using our VOFI-based [4] integration algorithm extended to four dimensions (recursive reconstruction and numerical integration over the resulting 4-polytopes).

Table 1 reports the convergence of the hypervolume integral for three representative 4D geometries: a hypersphere, a hyperellipsoid and a sinusoidal slab. The exact reference volumes are available in closed form for the hypersphere and the ellipsoid and for the sinusoidal slab they are obtained from its analytic definition; the corresponding values are listed in the table.

N	h	V_{num}	rel. err.	N	h	V_{num}	rel. err.
4	0.25	7.4053150e-2	3.7055e-6	4	0.25	8.3275552e-2	9.1814e-6
6	0.166666	7.4052876e-2	3.0536e-9	6	0.166666	8.3274857e-2	8.3516e-7
8	0.125	7.4052875e-2	1.7002e-9	8	0.125	8.3274787e-2	8.6144e-10
10	0.10	7.4052876e-2	1.1917e-10	10	0.10	8.3274787e-2	2.2451e-10
12	0.083333	7.4052876e-2	4.3828e-10	12	0.083333	8.3274787e-2	9.1379e-11
16	0.0625	7.4052876e-2	4.5370e-13	16	0.0625	8.3274787e-2	7.9042e-11
32	0.03125	7.4052876e-2	3.0266e-13	32	0.03125	8.3274787e-2	6.6589e-10

(a) **Hypersphere.**

N	h	V_{num}	rel. err.
4	0.25	6.0082800e-1	1.3800e-3
6	0.166666	5.9999988e-1	2.0558e-7
8	0.125	6.0000000e-1	1.4730e-9
10	0.10	6.0000000e-1	1.1591e-11
12	0.083333	6.0000000e-1	4.0708e-14
16	0.0625	6.0000000e-1	1.6098e-14
32	0.03125	6.0000000e-1	7.0684e-14

(b) **Hyperellipsoid.**

N	h	V_{num}	rel. err.
4	0.25	6.0082800e-1	1.3800e-3
6	0.166666	5.9999988e-1	2.0558e-7
8	0.125	6.0000000e-1	1.4730e-9
10	0.10	6.0000000e-1	1.1591e-11
12	0.083333	6.0000000e-1	4.0708e-14
16	0.0625	6.0000000e-1	1.6098e-14
32	0.03125	6.0000000e-1	7.0684e-14

(c) **Sinusoidal slab.**

N	h	V_{num}	rel. err.
4	0.25	6.0082800e-1	1.3800e-3
6	0.166666	5.9999988e-1	2.0558e-7
8	0.125	6.0000000e-1	1.4730e-9
10	0.10	6.0000000e-1	1.1591e-11
12	0.083333	6.0000000e-1	4.0708e-14
16	0.0625	6.0000000e-1	1.6098e-14
32	0.03125	6.0000000e-1	7.0684e-14

Table 1: Four-dimensional hypervolume integration for representative geometries. V_{num} is computed by the 4D geometric integration engine and “rel. err.” denotes $|V_{\text{num}} - V_{\text{ex}}|/|V_{\text{ex}}|$. Exact values: hypersphere $V_{\text{ex}} = 0.07405287552192358$, hyperellipsoid $V_{\text{ex}} = 0.08327478713419147$, sinusoidal slab $V_{\text{ex}} = 0.6$.

Across the curved geometries (hypersphere and ellipsoid), the hypervolume error drops by several orders of magnitude between coarse and moderate resolutions and reaches near round-off levels on the finest grids (e.g. absolute errors of $\mathcal{O}(10^{-14})$ for the hypersphere at $N \geq 16$). In this regime, observed orders become unreliable and may appear non-monotone because the error is dominated by floating-point effects and by the tolerance of the geometric predicates rather than by the mesh size. The sinusoidal slab exhibits the same behaviour on most grids (machine-level accuracy at $N = 8, 12, 16$), while a few intermediate resolutions show larger deviations; nevertheless, refinement recovers the expected high accuracy. Overall, these results validate the correctness and robustness of the four-dimensional clipping and integration pipeline that underpins the space-time moments used by the moving-domain operators.

5.2 2D diffusion with an oscillating circular boundary

We consider a transient diffusion problem in a circular domain whose boundary oscillates periodically in time. The background domain is the fixed box $\Omega_{\text{box}} = [0, 4]^2$ and the physical domain is

$$\Omega(t) = \{(x, y) \in \Omega_{\text{box}} : r(x, y) < R(t)\}, \quad r(x, y) = \|(x, y) - \mathbf{x}_c\|, \quad \mathbf{x}_c = (2, 2).$$

The radius follows the smooth motion

$$R(t) = R_{\text{mean}} + R_{\text{amp}} \sin\left(2\pi \frac{t}{T}\right), \quad (56)$$

with $R_{\text{mean}} = 1.0$, $R_{\text{amp}} = 0.5$ and $T = 1.0$. The moving boundary $\Gamma(t) = \partial\Omega(t)$ therefore sweeps through the Cartesian mesh and continuously generates fresh and dead cut cells over the simulation.

Inside $\Omega(t)$ we solve the diffusion equation

$$\partial_t \phi = D \Delta \phi + f(x, y, t), \quad (x, y) \in \Omega(t), \quad (57)$$

with constant diffusivity D and Dirichlet boundary conditions prescribed on the moving boundary,

$$\phi(x, y, t) = \phi_{\text{ex}}(x, y, t) \quad \text{on } \Gamma(t). \quad (58)$$

The pair (ϕ_{ex}, f) is manufactured so that ϕ_{ex} satisfies (57)-(58) exactly in the evolving domain; we use

$$\phi_{\text{ex}}(x, y, t) = R(t) \cos(\pi x) \cos(\pi y), \quad (59)$$

which yields the forcing term

$$f(x, y, t) = \cos(\pi x) \cos(\pi y) \left[\dot{R}(t) + 2\pi^2 D R(t) \right], \quad \dot{R}(t) = \frac{2\pi R_{\text{amp}}}{T} \cos\left(2\pi \frac{t}{T}\right). \quad (60)$$

We take $D = 0.1$, integrate to $t_f = T$ with $\Delta t = 0.25 \min(\Delta x, \Delta y)$ using a $\theta = 1/2$ midpoint scheme. Errors are evaluated at the final time t_f using cut-cell weighted L^2 norms over regular cells, cut cells and all cells. Table 2 reports the corresponding errors and observed convergence rates.

h	N_{diam}	$\ e(t_f)\ _{2,\text{reg}}$	$\ e(t_f)\ _{2,\text{cut}}$	$\ e(t_f)\ _{2,\text{all}}$	p_{reg}	p_{cut}	p_{all}
1.0	3	2.315e-1	1.598e0	1.615e0	-	-	-
0.5	6	1.496e-1	1.600e-1	2.191e-1	0.63	3.32	2.88
0.25	12	7.056e-2	3.532e-2	7.890e-2	1.08	2.18	1.47
0.125	24	2.780e-2	8.013e-3	2.893e-2	1.34	2.14	1.45
0.0625	42	1.210e-2	2.565e-3	1.237e-2	1.20	1.64	1.23
0.03125	84	5.368e-3	6.835e-4	5.411e-3	1.17	1.91	1.19
fit	-	-	-	-	1.21	1.95	1.34

Table 2: L^2 error at final time t_f for the oscillating-disk diffusion test.

Table 2 demonstrates a systematic reduction of the error under mesh refinement, on regular cells, on cut cells and on the full set of cells. Remarkably, the method remains robust even in the most under-resolved configuration ($N_{\text{diam}} = 3$), where the moving boundary sweeps through only a handful of cells and repeatedly generates fresh and dead cut cells within a single period. As expected, this regime produces large cut-cell errors but it constitutes a stringent stress test of the space-time balance in the presence of very small and rapidly evolving phase-restricted volumes.

Once the interface is better resolved ($h \leq 0.5$), the cut-cell contribution decreases rapidly and exhibits super-linear convergence, with an overall rate close to second order. On the finest grids, the cut-cell error becomes smaller than the regular-cell error, indicating that the space-time sweeping treatment and the fresh/dead-cell closure do not induce a degradation of accuracy near the moving boundary.

Figure 7 further confirms that the numerical solution remains smooth and bounded throughout the oscillation cycle, with no visible artifacts correlated with the creation or disappearance of cut cells. The solution matches the prescribed Dirichlet boundary condition along $\Gamma(t)$ at all phases, while the interior field evolves continuously during expansion and contraction, illustrating the robustness of the space-time flux balance across topology changes.

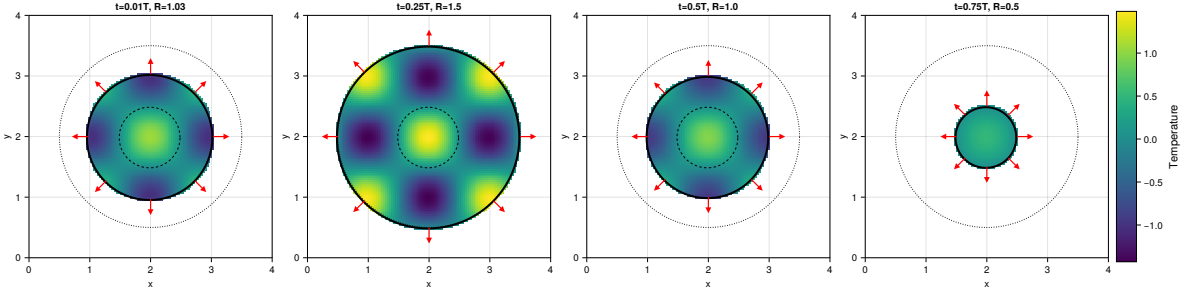


Figure 7: Snapshots at four phases of one oscillation period ($t = 0, T/4, T/2, 3T/4$). The solid curve shows the exact moving boundary $r = R(t)$ and the colormap shows the numerical solution ϕ .

5.3 2D Diffusion with multiple bodies (McCorquodale-Colella)

We consider the two-dimensional moving-interface benchmark of McCorquodale and Colella [15], in which several rigid ellipses translate with prescribed velocities inside a fixed Cartesian box. The background domain is the fixed Cartesian box $\Omega_{\text{box}} = [-1.5, 1.5] \times [-1.0, 1.0]$, and the time-dependent physical domain is obtained by removing the interiors of three moving ellipses,

$$\Omega(t) = \Omega_{\text{box}} \setminus \bigcup_{k=1}^3 E_k(t), \quad \Gamma(t) = \partial\Omega(t) = \partial\Omega_{\text{box}} \cup \bigcup_{k=1}^3 \Gamma_k(t),$$

where $\Gamma_k(t) = \partial E_k(t)$ denotes the boundary of ellipse k . As the ellipses translate across the mesh, the interface $\Gamma(t)$ sweeps through cells and repeatedly creates fresh and dead cut cells.

Let $\gamma = \sqrt{2}/15$. At $t = 0$, ellipse k is defined by its center (x_k^0, y_k^0) and semi-axes (a_k, b_k) ,

$$\begin{aligned} (x_1^0, y_1^0, a_1, b_1) &= (-6\gamma, -5\gamma, 3\gamma, 2\gamma), \\ (x_2^0, y_2^0, a_2, b_2) &= (10\gamma, -7\gamma, 2\gamma, \gamma), \\ (x_3^0, y_3^0, a_3, b_3) &= (7\gamma, 3\gamma, 1.5\gamma, 2\gamma). \end{aligned}$$

and translated with constant velocities

$$(u_1, v_1) = (-0.10, 0.20), \quad (u_2, v_2) = (-0.15, 0.15), \quad (u_3, v_3) = (-0.20, 0.20).$$

Thus, the ellipse centers evolve as

$$x_k(t) = x_k^0 + u_k t, \quad y_k(t) = y_k^0 + v_k t,$$

and the moving boundaries are

$$\Gamma_k(t) = \left\{ (x, y) : \left(\frac{x - x_k(t)}{a_k} \right)^2 + \left(\frac{y - y_k(t)}{b_k} \right)^2 = 1 \right\}.$$

On $\Omega(t)$ we solve the transient diffusion problem

$$\partial_t \phi = \Delta \phi + f(x, y, t), \quad (x, y) \in \Omega(t), \quad (61)$$

with Dirichlet boundary conditions prescribed on the entire boundary $\Gamma(t)$,

$$\phi(x, y, t) = \phi_{\text{ex}}(x, y, t) \quad \text{on } \Gamma(t). \quad (62)$$

The manufactured reference field and corresponding forcing are chosen as

$$\phi_{\text{ex}}(x, y, t) = \frac{4}{5\pi(t+1)} \exp\left(-\frac{x^2 + y^2}{5(t+1)}\right), \quad (63)$$

$$f(x, y, t) = \frac{4(x^2 + y^2 - 5(t+1))}{125\pi(t+1)^3} \exp\left(-\frac{x^2 + y^2}{5(t+1)}\right), \quad (64)$$

h	N_{diam}	$\ e(t_f)\ _{2,\text{reg}}$	$\ e(t_f)\ _{2,\text{cut}}$	$\ e(t_f)\ _{2,\text{all}}$	p_{reg}	p_{cut}	p_{all}
0.50	1	-	-	-	-	-	-
0.22	2	-	4.509e-3	4.509e-3	-	-	-
0.125	4	8.410e-4	1.786e-3	1.974e-3	-	1.61	1.44
0.0606	7	4.053e-4	3.902e-4	5.626e-4	1.01	2.10	1.73
0.0317	12	1.146e-4	1.108e-4	1.594e-4	1.95	1.95	1.95
0.0157	24	3.620e-5	3.380e-5	4.953e-5	1.64	1.69	1.67
fit	-	-	-	-	1.55	1.89	1.74

Table 3: L_2 error at final time t_f for the McCrorquodale-Colella moving-ellipses Dirichlet test.

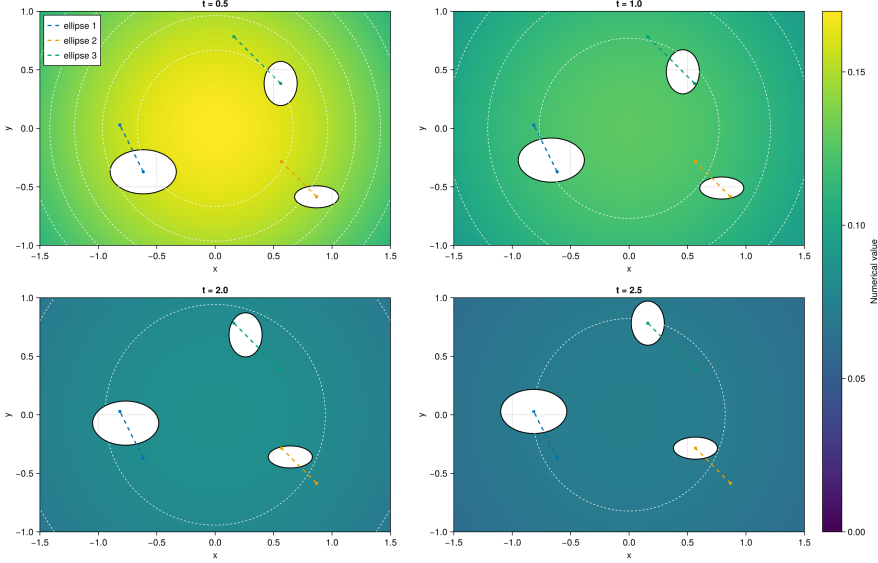


Figure 8: Snapshots of the moving-ellipses test at four instants ($t = 0.5$, $t = 1.0$, $t = 2.0$, $t = 2.5$). The solid curves show the translated elliptic boundaries $\Gamma_k(t)$ and the colormap shows the numerical solution ϕ .

so that (63) satisfies (61)-(62) exactly in the moving domain.

Table 3 reports the cut-cell weighted L^2 error at final time t_f , split into regular cells, cut cells and all cells. Here N_{diam} denotes the number of cells per characteristic domain diameter.

The two coarsest meshes are severely under-resolved (few cells per ellipse), yet the method remains robust and produces a bounded solution while the three bodies translate and continuously trigger fresh/dead cut-cell events. From $h \leq 0.125$ onward, the errors decrease systematically on both regular and cut-cell subsets. The cut-cell error exhibits a clear super-linear regime and approaches second-order behaviour under refinement, leading to an overall least-squares rate close to two on the finest levels (Table 3). The comparable decay of $\|e\|_{2,\text{reg}}$ and $\|e\|_{2,\text{cut}}$ indicates that the space-time sweeping treatment and the moving Dirichlet enforcement do not degrade accuracy near the translating boundaries. This test also exercises the simultaneous handling of multiple embedded bodies: three distinct ellipses translate concurrently and contribute to the global set of cut cells. The solver remains robust in this multi-body configuration. Figure 8 shows smooth snapshots across the trajectory, with no visible artifacts correlated with the repeated creation and removal of cut cells.

5.4 3D Schwartz-Colella diffusion on an expanding sphere

We reproduce the three-dimensional moving-boundary benchmark of Schwartz and Colella [18], in which diffusion is solved in a domain bounded by a prescribed expanding sphere. The background domain is the fixed Cartesian box $\Omega_{\text{box}} = [-1, 1]^3$, while the physical domain is the time-dependent ball

$$\Omega(t) = \{(x, y, z) \in \Omega_{\text{box}} : r(x, y, z) < R(t)\}, \quad r(x, y, z) = \|(x, y, z)\|, \quad R(t) = 0.392 + t,$$

with moving boundary $\Gamma(t) = \partial\Omega(t) = \{r = R(t)\}$. The interface motion sweeps through the mesh and continuously creates fresh and dead cut cells over the simulation interval.

Inside $\Omega(t)$ we solve the transient diffusion equation

$$\partial_t \phi = \Delta \phi + f(x, y, z, t), \quad (x, y, z) \in \Omega(t), \quad (65)$$

with Dirichlet boundary conditions prescribed on the immersed boundary,

$$\phi(x, y, z, t) = \phi_{\text{ex}}(x, y, z, t) \quad \text{on } \Gamma(t). \quad (66)$$

The manufactured reference field is chosen as

$$\phi_{\text{ex}}(x, y, z, t) = \frac{4}{5\pi(t+1)} \exp\left(-\frac{x^2 + y^2 + z^2}{5(t+1)}\right), \quad (67)$$

and the forcing term is

$$f(x, y, z, t) = \frac{4(x^2 + y^2 + z^2 + 5(t+1))}{125\pi(t+1)^3} \exp\left(-\frac{x^2 + y^2 + z^2}{5(t+1)}\right), \quad (68)$$

so that (67) satisfies (65)-(66) exactly in the evolving domain.

Errors are evaluated at the final time t_f using cut-cell weighted L^2 norms over regular cells, cut cells and all active cells. Table 4 reports the corresponding errors and pairwise observed orders under refinement.

h	N_{in}	$\ e(t_f)\ _{2,\text{all}}$	$\ e(t_f)\ _{2,\text{reg}}$	$\ e(t_f)\ _{2,\text{cut}}$	p_{all}	p_{reg}	p_{cut}
0.25	18	1.4110e-2	7.5513e-3	1.19198e-2	-	-	-
0.125	147	6.9784e-3	5.8039e-3	3.8745e-3	1.016	0.380	1.621
0.083333	611	4.0096e-3	3.6258e-3	1.7121e-3	1.367	1.160	2.014
0.0625	1479	2.7139e-3	2.5211e-3	1.0047e-3	1.357	1.263	1.853
fit	-	-	-	-	1.36	1.20	1.95

Table 4: L^2 error at final time t_f for the 3D Schwartz–Colella expanding-sphere test. Errors are split into contributions from all active cells, regular cells and cut cells. Here N_{in} denotes the number of active cells inside the sphere.

The method remains stable while the sphere expands and sweeps across the Cartesian mesh, continuously creating fresh cut cells near $\Gamma(t)$. Table 4 shows consistent error reduction under refinement for all three subsets. The global error $\|e\|_{2,\text{all}}$ exhibits super-linear convergence. Cut-cell errors converge even faster (orders $\approx 1.6\text{--}2.0$), indicating that the space-time sweeping treatment and the fresh/dead-cell closure do not degrade accuracy near the moving boundary. The regular-cell contribution converges more slowly on the coarsest refinement but approaches a super-linear regime as the sphere becomes better resolved.

5.5 Manufactured solution with an oscillating two-phase interface

To assess the accuracy and robustness of the moving two-phase solver, we design a manufactured configuration with a time-periodic vertical sharp interface. The computational box is $\Omega = [0, 4]^2$ and the interface location is prescribed as

$$s(t) = s_0 + A \sin(\omega t), \quad (69)$$

so that the moving interface is $\Gamma(t) = \{x = s(t)\}$ and the two phases are

$$\Omega^-(t) = \{(x, y) \in \Omega : x < s(t)\}, \quad \Omega^+(t) = \{(x, y) \in \Omega : x > s(t)\}.$$

We use the unit normal $\mathbf{n} = (1, 0)$ pointing from $\Omega^-(t)$ to $\Omega^+(t)$, hence $\partial_n = \partial_x$ and the prescribed normal velocity is

$$w(t) = \dot{s}(t) = A\omega \cos(\omega t). \quad (70)$$

In each phase we solve the transient diffusion model

$$c_p^\pm \partial_t \phi^\pm = \nabla \cdot (D^\pm \nabla \phi^\pm) + f^\pm(x, y, t), \quad (x, y) \in \Omega^\pm(t), \quad (71)$$

with Dirichlet boundary conditions on the outer boundary. Across $\Gamma(t)$ we impose the two-fluid coupling conditions

$$[\phi] = 0, \quad [D \partial_n \phi] = 0, \quad \text{on } \Gamma(t), \quad (72)$$

corresponding to continuity of temperature and diffusive heat flux, with no interfacial storage or sources.

We choose phase fields of the form

$$\phi^\pm(x, y, t) = A^\pm (x - s(t)) x (4 - x) y (4 - y) e^{-t}, \quad (73)$$

with the coefficients $A^- = D^+, A^+ = D^-$. This construction enforces $\phi^\pm = 0$ on $\partial\Omega$ and also $[\phi] = 0$. Moreover,

$$\partial_x \phi^\pm(s(t), y, t) = A^\pm s(t) (4 - s(t)) y (4 - y) e^{-t},$$

so that the choice $A^- = D^+$ and $A^+ = D^-$ yields $D^- \partial_x \phi^-(s(t), y, t) = D^+ \partial_x \phi^+(s(t), y, t)$, i.e. $[D \partial_n \phi] = 0$.

The forcing terms are defined analytically by substitution of (73) into (71),

$$f^\pm(x, y, t) = c_p^\pm \partial_t \phi^\pm - \nabla \cdot (D^\pm \nabla \phi^\pm), \quad (74)$$

with $\partial_t \phi^\pm$ containing the interface-motion contribution through $s'(t) = A\omega \cos(\omega t)$. In particular, increasing ω directly amplifies the time-dependent part of the forcing and increases the sweeping speed $|w(t)|$, thus intensifying the creation/removal of cut cells and making the test more demanding for the space-time update.

In the results below we take $c_p^\pm = 1, D^- = 0.1, D^+ = 1.0, s_0 = 2, A = 1$, integrate to a final time $t_f = 0.5$ with a midpoint time scheme and measure cut-cell weighted L^2 errors at t_f over regular cells, cut cells and all active cells. As $\Gamma(t)$ oscillates, both phases repeatedly generate fresh and dead cut cells, providing a direct validation of the space-time two-phase coupling in the presence of topology changes.

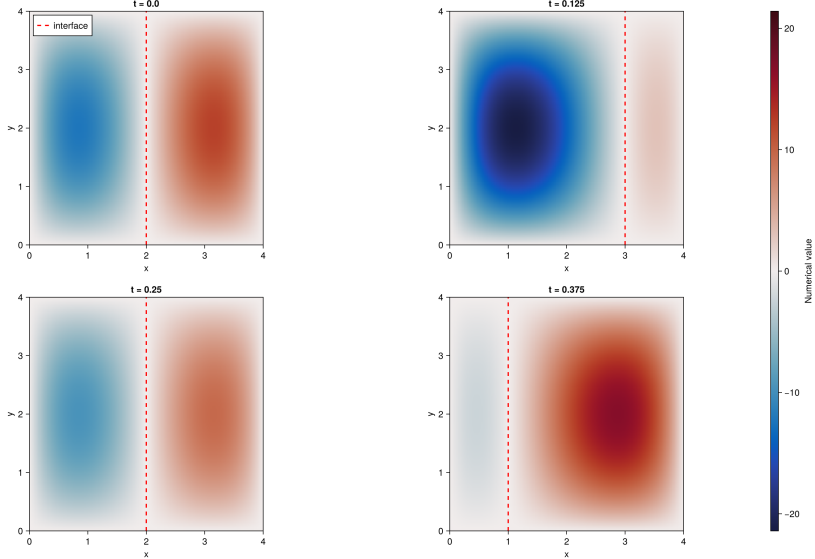


Figure 9: Snapshots of the moving vertical interface test at four instants ($t = 0, t = 0.125, t = 0.25, t = 0.375$). The red dashed line shows the prescribed moving boundary and the colormap represents ϕ on planar slices.

Table 5 reports the errors and pairwise observed orders on a sequence of $N \times N$ grids.

The global error decreases monotonically with refinement and enters an approximately second-order regime on the finest levels. The cut-cell error converges faster than the regular-cell contribution on refined grids, showing that the space-time sweeping treatment and the two-phase coupling across $\Gamma(t)$ remain accurate despite repeated creation and removal of phase-restricted volumes.

To probe robustness with respect to interface speed, we repeat the same manufactured two-phase test while increasing the oscillation frequency ω in $s(t) = s_0 + A \sin(\omega t)$ (and thus the normal velocity $w(t) = A\omega \cos(\omega t)$). Increasing ω directly amplifies the time-dependent component of the forcing through $s'(t)$ and increases the sweeping speed $|w(t)|$, thereby intensifying the creation/removal of cut cells within each time slab.

h	$\ e(t_f)\ _{2,\text{reg}}$	$\ e(t_f)\ _{2,\text{cut}}$	$\ e(t_f)\ _{2,\text{all}}$	p_{reg}	p_{cut}	p_{all}
1.0	2.3827e-1	3.0388e-1	3.8616e-1	-	-	-
0.5	1.9904e-1	1.8845e-1	2.5577e-1	0.26	0.69	0.59
0.25	8.4559e-2	5.9272e-2	9.1495e-2	1.24	1.67	1.48
0.125	2.8215e-2	1.6183e-2	3.0286e-2	1.58	1.87	1.60
0.0625	8.0159e-3	2.3389e-3	8.2765e-3	1.82	2.79	1.87
0.03125	2.1327e-3	4.5489e-4	2.1614e-3	1.91	2.36	1.94
fit	-	-	-	1.86	2.58	1.90

Table 5: L^2 error and convergence rates for the manufactured oscillating two-phase vertical-interface test.

Tables 6-7 summarize the results. For moderate frequencies ($\omega \leq 8\pi$), the global error $\|e(t_f)\|_{2,\text{all}}$ decreases monotonically with refinement and enters a near second-order regime on the finest grids, with least-squares rates $p_{\text{all}} \approx 1.6\text{-}1.9$. The cut-cell contribution remains superlinear, showing that the space-time sweeping treatment and two-fluid coupling across $\Gamma(t)$ do not degrade accuracy at the moving interface despite repeated fresh/dead events. As ω increases further, the fitted global rate decreases (e.g. around $p_{\text{all}} \approx 1.2$ at $\omega = 16\pi$ on the same fine-grid window), which is consistent with the test becoming more demanding due to faster geometry motion and stronger time-dependent forcing. At $\omega = 32\pi$, the error is not monotone across the three finest grids, so a single asymptotic spatial rate is not meaningful; nonetheless, the solution remains stable and bounded and the finest-grid errors remain comparable to the lower-frequency cases.

ω	$\ e(t_f)\ _{2,\text{all}}(h_{\min})$	$\ e(t_f)\ _{2,\text{reg}}(h_{\min})$	$\ e(t_f)\ _{2,\text{cut}}(h_{\min})$	p_{all}	p_{reg}	p_{cut}
2π	2.1614e-3	2.1327e-3	4.5489e-4	1.90	1.86	2.58
4π	2.1577e-3	2.1206e-3	3.9829e-4	1.83	1.82	2.46
8π	1.9600e-3	1.9342e-3	4.1152e-4	1.62	1.59	2.26
16π	1.6749e-3	1.6481e-3	2.9868e-4	1.19	1.16	1.86
32π	9.0455e-4	8.9578e-4	1.6759e-4	-	-	-

Table 6: Frequency sweep for the manufactured oscillating two-phase interface. Reported errors are at the finest mesh $h_{\min} = 0.03125$. Least-squares orders are fitted over $h \in \{0.125, 0.0625, 0.03125\}$. For $\omega = 32\pi$, the error is not monotone on this window, hence no single fit is reported.

ω	$h = 0.125$			$h = 0.03125$		
	$\ e\ _{2,\text{all}}$	$\ e\ _{2,\text{reg}}$	$\ e\ _{2,\text{cut}}$	$\ e\ _{2,\text{all}}$	$\ e\ _{2,\text{reg}}$	$\ e\ _{2,\text{cut}}$
2π	3.0286e-2	2.8215e-2	1.6183e-2	2.1614e-3	2.1327e-3	4.5489e-4
4π	2.7262e-2	2.6297e-2	1.2065e-2	2.1577e-3	2.1206e-3	3.9829e-4
8π	1.8595e-2	1.7534e-2	9.4710e-3	1.9600e-3	1.9342e-3	4.1152e-4
16π	8.7483e-3	8.2674e-3	3.9314e-3	1.6749e-3	1.6481e-3	2.9868e-4
32π	6.0882e-4	4.3472e-4	4.2623e-4	9.0455e-4	8.9578e-4	1.6759e-4

Table 7: Errors versus oscillation frequency at two representative mesh sizes. The $\omega = 32\pi$ case illustrates a non-monotone trend on fine grids, typical of a very demanding sweeping regime.

6 Conclusions and outlook

This work extends our Cartesian cut-cell finite-volume framework to prescribed moving geometries through a space-time formulation. Over each time slab $[t_n, t_{n+1}]$, the evolving control volumes are treated as $(d+1)$ -dimensional space-time cut cells and all geometric moments (volumes, apertures and auxiliary moments) are replaced by their time-integrated counterparts. Starting from Reynolds' transport theorem, we derived fully conservative discrete balances in which the interface motion appears as

an interface contribution that is closed by a geometric conservation law. This construction preserves the static algebraic structure: the same local divergence/gradient operators are reused, with only the geometric measures modified.

A first contribution is the geometric backbone required by the space-time operators. We showed that the moment-based machinery lifts naturally to higher-dimensional integration and validated a 4D volume/surface integration engine on representative hypershapes (hypersphere, hyperellipsoid and a sinusoidal slab). The results confirm that the extended VOFI-based integration engine provides accurate hypervolume measures under refinement and is suitable for assembling the time-integrated moments that drive the moving cut-cell scheme.

A second contribution is a robust treatment of topology changes within a time step. Fresh and dead cut cells arise when the interface sweeps across a fixed mesh. We introduced a state-dependent closure that keeps the space-time constitutive fluxes well-defined even when one endpoint phase volume vanishes, while maintaining conservation. Across all moving benchmarks, no special-case remeshing or ad hoc mass fixes are required: the conservative update follows directly from the space-time boundary fluxes.

The numerical validation suite supports these claims on increasingly demanding moving configurations. In the monophasic oscillating-disk diffusion problem, the method remains stable and bounded even in an under-resolved regime with only a few points across the diameter, while exhibiting rapid error reduction once the interface is better resolved. The McCorquodale-Colella moving-ellipses test demonstrates that multiple translating bodies with different aspect ratios can be handled simultaneously, recovering essentially second-order convergence when the motion is smooth. In three dimensions, the Schwartz-Colella expanding-sphere benchmark confirms that the space-time construction extends directly to $d = 3$: errors decrease systematically with refinement and the cut-cell contribution converges at least as fast as the regular region, indicating that the time-integrated geometric weights do not degrade accuracy near the moving embedded boundary. Finally, the two-phase manufactured test validates the full moving two-fluid coupling: continuity of the scalar and of the diffusive normal flux is enforced across $\Gamma(t)$ while both phases experience repeated fresh/dead events. The observed convergence approaches second order on refined meshes and additional runs with increasing oscillation frequency show that the solver remains robust as the sweeping speed and the temporal stiffness of the forcing increase.

Overall, the moving-geometry results draw a coherent picture: the proposed space-time cut-cell formulation (i) preserves constant states through a discrete geometric conservation law, (ii) maintains global conservation across topology changes within a time step, (iii) remains robust on severely under-resolved moving geometries and (iv) achieves super-linear convergence in practical moving-interface benchmarks in 2D and 3D, including multiple-body motion and two-phase coupling. These properties provide the essential numerical building blocks for more complex sharp-interface multiphysics.

The most natural next step is to move from prescribed motion to free-boundary dynamics, where interface velocity is determined by physics rather than imposed. The present space-time machinery is directly aligned with Stefan-type phase-change models: the method already provides conservative phase balances, accurate approximations of normal fluxes on moving interfaces and a robust handling of discrete events as small phase volumes appear or vanish. Beyond pure diffusion, extending the framework to advection-diffusion and to incompressible two-phase Navier-Stokes with sharp interfaces would enable fully coupled problems with density/viscosity jumps, interfacial stress continuity and thermal/mass transfer. In that setting, the time-integrated geometric operators developed here can be reused for diffusive and elliptic (pressure) terms, while additional space-time consistent cut-cell operators are required for convection and for interface-consistent momentum coupling. On the numerical side, an important direction is to strengthen the coupling between interface advancement and the bulk PDE solves. In the present study, the geometry is prescribed but in free-boundary settings the interface location and the interfacial fluxes must be updated consistently within each time step. This calls for tighter interface-tracking strategies together with coupled or iterative interface-PDE algorithms that enforce the jump conditions and the interface kinetics (e.g. Stefan-type laws) at the discrete level. This will make the method a practical tool for large-scale, interface-resolved free-boundary multiphysics.

A Summary table for Space-time quantities notations

Quantity	Definition using $\langle \cdot, \cdot \rangle$	Equivalent integral form
T-i cell volume	$\mathcal{V}_{n+1/2,i,j}^{\pm} = \langle]t_n, t_{n+1}[, V_{i,j}^{\pm}(t) \rangle$	$\int_{t_n}^{t_{n+1}} \int_{\Omega_{i,j}^{\pm}(t)} 1 \, dV \, dt$
T-i face area (x -normal)	$\mathcal{A}_{n+1/2,i-1/2,j}^{1\pm} = \langle]t_n, t_{n+1}[, A_{i-1/2,j}^{1\pm}(t) \rangle$	$\int_{t_n}^{t_{n+1}} \int_{\Sigma_j^{1\pm}(t, x_{i-1/2})} 1 \, dS \, dt$
T-i face area (y -normal)	$\mathcal{A}_{n+1/2,i,j-1/2}^{2\pm} = \langle]t_n, t_{n+1}[, A_{i,j-1/2}^{2\pm}(t) \rangle$	$\int_{t_n}^{t_{n+1}} \int_{\Sigma_i^{2\pm}(t, y_{j-1/2})} 1 \, dS \, dt$
T-a cell centroid (x -coord.)	$\mathcal{X}_{n+1/2,i,j}^{\pm} = \frac{\langle]t_n, t_{n+1}[, \langle \Omega_{i,j}^{\pm}(t), x \rangle \rangle}{\mathcal{V}_{n+1/2,i,j}^{\pm}}$	$\frac{\int_{t_n}^{t_{n+1}} \int_{\Omega_{i,j}^{\pm}(t)} x \, dV \, dt}{\int_{t_n}^{t_{n+1}} \int_{\Omega_{i,j}^{\pm}(t)} dV \, dt}$
T-a cell centroid (y -coord.)	$\mathcal{Y}_{n+1/2,i,j}^{\pm} = \frac{\langle]t_n, t_{n+1}[, \langle \Omega_{i,j}^{\pm}(t), y \rangle \rangle}{\mathcal{V}_{n+1/2,i,j}^{\pm}}$	$\frac{\int_{t_n}^{t_{n+1}} \int_{\Omega_{i,j}^{\pm}(t)} y \, dV \, dt}{\int_{t_n}^{t_{n+1}} \int_{\Omega_{i,j}^{\pm}(t)} dV \, dt}$
T-i centroidal face area (x -dir.)	$\mathcal{B}_{n+1/2,i,j}^{1\pm} = \langle]t_n, t_{n+1}[, \langle \Sigma_j^{1\pm}(t, \mathcal{X}_{n+1/2,i,j}^{\pm}), 1 \rangle \rangle$	$\int_{t_n}^{t_{n+1}} \int_{\Sigma_j^{1\pm}(t, \mathcal{X}_{n+1/2,i,j}^{\pm})} 1 \, dS \, dt$
T-i centroidal face area (y -dir.)	$\mathcal{B}_{n+1/2,i,j}^{2\pm} = \langle]t_n, t_{n+1}[, \langle \Sigma_i^{2\pm}(t, \mathcal{Y}_{n+1/2,i,j}^{\pm}), 1 \rangle \rangle$	$\int_{t_n}^{t_{n+1}} \int_{\Sigma_i^{2\pm}(t, \mathcal{Y}_{n+1/2,i,j}^{\pm})} 1 \, dS \, dt$
T-i staggered volume (x -dir.)	$\mathcal{W}_{n+1/2,i-1/2,j}^{1\pm} = \langle]t_n, t_{n+1}[, \langle \mathcal{X}_{n+1/2,i-1/2,j}^{\pm}, \mathcal{X}_{n+1/2,i,j}^{\pm} \rangle \rangle_{\times [y_{j-1/2}, y_{j+1/2}] \cap \Omega^{\pm}(t), 1}$	$\int_{t_n}^{t_{n+1}} \int_{(\cdot) \cap \Omega^{\pm}(t)} 1 \, dV \, dt$
T-i staggered volume (y -dir.)	$\mathcal{W}_{n+1/2,i,j-1/2}^{2\pm} = \langle]t_n, t_{n+1}[, \langle \mathcal{Y}_{n+1/2,i,j-1}^{\pm}, \mathcal{Y}_{n+1/2,i,j}^{\pm} \rangle \rangle_{\times [y_{j-1/2}, y_{j+1/2}] \cap \Omega^{\pm}(t), 1}$	$\int_{t_n}^{t_{n+1}} \int_{(\cdot) \cap \Omega^{\pm}(t)} 1 \, dV \, dt$
S-t averaged bulk variable	$\tilde{\Phi}_{i,j}^{\omega\pm} = \frac{\langle]t_n, t_{n+1}[, \langle \Omega_{i,j}^{\pm}(t), \phi^{\pm}(t) \rangle \rangle}{\mathcal{V}_{n+1/2,i,j}^{\pm}}$	$\frac{\int_{t_n}^{t_{n+1}} \int_{\Omega_{i,j}^{\pm}(t)} \phi^{\pm}(t) \, dV \, dt}{\int_{t_n}^{t_{n+1}} \int_{\Omega_{i,j}^{\pm}(t)} dV \, dt}$
S-t averaged flux (x -dir.)	$\mathcal{Q}_{n+1/2,i+1/2,j}^{1\pm} = \frac{\langle]t_n, t_{n+1}[, \langle \Sigma_j^{1\pm}(x_{i+1/2}), q^{1\pm} \rangle \rangle}{\mathcal{A}_{n+1/2,i+1/2,j}^{1\pm}}$	$\frac{\int_{t_n}^{t_{n+1}} \int_{\Sigma_j^{1\pm}(t, x_{i+1/2})} q^{1\pm}(t) \, dS \, dt}{\int_{t_n}^{t_{n+1}} \int_{\Sigma_j^{1\pm}(t, x_{i+1/2})} dS \, dt}$
S-t averaged source term	$\mathcal{R}_{n+1/2,i,j}^{\pm} = \frac{\langle]t_{n+1}, t_{n+1}[, \langle \Omega_{i,j}^{\pm}(t), r^{\pm}(t) \rangle \rangle}{\mathcal{V}_{n+1/2,i,j}^{\pm}}$	$\frac{\int_{t_{n+1}}^{t_{n+1}} \int_{\Omega_{i,j}^{\pm}(t)} r^{\pm}(t) \, dV \, dt}{\int_{t_{n+1}}^{t_{n+1}} \int_{\Omega_{i,j}^{\pm}(t)} dV \, dt}$
S-t interface field average	$\mathcal{F}_{i,j}(t) = \frac{\langle]t_{n+1}, t_{n+1}[, \langle \Gamma_{i,j}(t), f(t) \rangle \rangle}{\int_{\Gamma_{i,j}(t)} 1 \, dS \, dt}$	$\frac{\int_{t_n}^{t_{n+1}} \int_{\Gamma_{i,j}(t)} f(t) \, dS \, dt}{\int_{t_n}^{t_{n+1}} \int_{\Gamma_{i,j}(t)} dS \, dt}$

Table 8: Summary of space-time geometric quantities and semi-discrete averages expressed using nested integral notation $\langle]t_n, t_{n+1}[, \langle \Xi(t), f(t) \rangle \rangle$. T-i stands for "Time-integrated", T-a for "Time-averaged" and S-t for "Space-time"

References

- [1] Vasilios Alexiades and Alan D. Solomon. *Mathematical Modeling of Melting and Freezing Processes*. Routledge, 1 edition, May 2018.
- [2] Robert Byron Bird, Warren E. Stewart, and Edwin N. Lightfoot. *Transport phenomena*. Wiley, New York, revised ed edition, 2007.
- [3] Donna Calhoun and Randall J. LeVeque. A Cartesian Grid Finite-Volume Method for the Advection-Diffusion Equation in Irregular Geometries. *Journal of Computational Physics*, 157(1):143–180, January 2000.
- [4] A. Chierici, L. Chirco, V. Le Chenadec, R. Scardovelli, Ph. Yecko, and S. Zaleski. An optimized Vof library to initialize the volume fraction field. *Computer Physics Communications*, 281:108506, December 2022.
- [5] C. Farhat, P. Geuzaine, and C. Grandmont. The Discrete Geometric Conservation Law and the Nonlinear Stability of ALE Schemes for the Solution of Flow Problems on Moving Grids. *Journal of Computational Physics*, 174(2):669–694, December 2001. Farhat2001.
- [6] James Gabbard and Wim M. Van Rees. A high-order finite difference method for moving immersed domain boundaries and material interfaces. *Journal of Computational Physics*, 507:112979, June 2024.
- [7] Frederic Gibou, Ronald P. Fedkiw, Li-Tien Cheng, and Myungjoo Kang. A Second-Order-Accurate Symmetric Discretization of the Poisson Equation on Irregular Domains. *Journal of Computational Physics*, 176(1):205–227, February 2002.
- [8] Roland Glowinski, Tsorng-Whay Pan, and Jacques Periaux. A fictitious domain method for Dirichlet problem and applications. *Computer Methods in Applied Mechanics and Engineering*, 111(3-4):283–303, January 1994.
- [9] Jonathan Ho and Charbel Farhat. Discrete embedded boundary method with smooth dependence on the evolution of a fluid-structure interface. *International Journal for Numerical Methods in Engineering*, 122(19):5353–5383, October 2021.
- [10] T.J.R. Hughes, J.A. Cottrell, and Y. Bazilevs. Isogeometric analysis: CAD, finite elements, NURBS, exact geometry and mesh refinement. *Computer Methods in Applied Mechanics and Engineering*, 194(39-41):4135–4195, October 2005.
- [11] Hans Johansen and Phillip Colella. A Cartesian Grid Embedded Boundary Method for Poisson’s Equation on Irregular Domains. *Journal of Computational Physics*, 147(1):60–85, November 1998.
- [12] Louis Libat, Can Selçuk, Eric Chénier, and Vincent Le Chenadec. A Cartesian Cut-Cell Two-Fluid Method for Two-Phase Diffusion Problems, December 2025. arXiv:2512.19407.
- [13] D. J. Mavriplis. Unstructured mesh generation and adaptivity. April 1995.
- [14] Peter McCorquodale and Phillip Colella. A high-order finite-volume method for conservation laws on locally refined grids. *Communications in Applied Mathematics and Computational Science*, 6(1):1–25, March 2011.
- [15] Peter McCorquodale, Phillip Colella, and Hans Johansen. A Cartesian Grid Embedded Boundary Method for the Heat Equation on Irregular Domains. *Journal of Computational Physics*, 173(2):620–635, November 2001.
- [16] Rajat Mittal and Gianluca Iaccarino. IMMERSED BOUNDARY METHODS. *Annual Review of Fluid Mechanics*, 37(1):239–261, January 2005.
- [17] Charles S Peskin. Flow patterns around heart valves: A numerical method. *Journal of Computational Physics*, 10(2):252–271, October 1972.
- [18] Peter Schwartz, Michael Barad, Phillip Colella, and Terry Ligocki. A Cartesian grid embedded boundary method for the heat equation and Poisson’s equation in three dimensions. *Journal of Computational Physics*, 211(2):531–550, January 2006.

- [19] J. Stefan. Ueber die Theorie der Eisbildung, insbesondere über die Eisbildung im Polarmeere. *Annalen der Physik*, 278(2):269–286, January 1891.
- [20] Kunihiko Taira and Tim Colonius. The immersed boundary method: A projection approach. *Journal of Computational Physics*, 225(2):2118–2137, August 2007.
- [21] Domingo Alberto Tarzia. A bibliography on moving-free boundary problems for the heat-diffusion equation. The stefan and related problems. *MAT Serie A*, 2:1–297, July 2000.